Published by Institute of Physics Publishing for SISSA
Received: *June 10, 2008*
Accepted: *June 28, 2008*
Published: *July 11, 2008*

JHEP07(2008)060

NLO vector-boson production matched with shower in POWHEG

Simone Alioli,[ab] **Paolo Nason,**[b] **Carlo Oleari**[ab] **and Emanuele Re**[ab]

[a] *Università di Milano-Bicocca,*
Piazza della Scienza 3, 20126 Milan, Italy
[b] *INFN, Sezione di Milano-Bicocca,*
Piazza della Scienza 3, 20126 Milan, Italy
E-mail: Simone.Alioli@mib.infn.it, Paolo.Nason@mib.infn.it, Carlo.Oleari@mib.infn.it, Emanuele.Re@mib.infn.it

Abstract: We present a next-to-leading-order calculation of W/Z production interfaced to shower Monte Carlo, implemented according to the POWHEG method. Finite width effects, Z/γ interference and angular correlations of decay products are included. A detailed comparison with MC@NLO and PYTHIA is carried out.

Keywords: NLO Computations, Hadronic Colliders, QCD.

Contents

JHEP07(2008)060

1. Introduction

The POWHEG method, first suggested in ref. [1], has been successfully applied to Z pair production [2], heavy-flavour production [3] and e^+e^- annihilation into hadrons [4]. In ref. [5] a general description of the method was given, and in particular its implementation within the Catani-Seymour (CS) subtraction scheme [6] and within the Frixione-Kunszt-Signer (FKS) [7, 8] approach.

In this paper we present an implementation of the W and Z hadroproduction cross section in the POWHEG framework, using the CS subtraction formalism. All next-to-leading-order (NLO) calculations used in POWHEG until now have been performed in the FKS method. In view of the popularity of the CS scheme, we find desirable to explore more in detail its use within POWHEG. In ref. [5] an outline of the implementation of the Drell-Yan production cross section in POWHEG in the CS scheme was given. In the present work we depart slightly from that approach. In particular, we use a more appropriate form of the

hardness variable used for the generation of radiation. As a further point, for the case of W production, if angular correlations in decay products are correctly taken into account, a new problem arises. In fact, the Born-level W cross section vanishes when the fermion decay products are exactly in the opposite direction of the incoming quark-antiquark pair, which causes a problem in the generation of radiation within the POWHEG method. We show that this problem has a simple solution, that can be easily generalized to all cases in which the Born cross section vanishes.

The paper is organized as follows. In section 2 we describe how we performed the calculation for the NLO W and Z cross section. In section 3 we discuss the POWHEG implementation and how to deal with vanishing Born cross sections. In section 4 we show our results for several kinematic variables and compare them with MC@NLO [9] and PYTHIA 6.4 [10]. Finally, in section 5, we give our conclusions.

2. Description of the calculation

2.1 Kinematics

2.1.1 Born kinematics

We begin by considering the Born process for the annihilation of a quark and an antiquark into a lepton-antilepton pair[1] $q + \bar{q} \to l + \bar{l}$. Following ref. [5], we denote by $k_\oplus$ and $k_\ominus$ the incoming quark momenta, and by k_1 and k_2 the outgoing fermion momenta. We call $K_\oplus$ and $K_\ominus$ the incoming hadron momenta and define the momentum fractions $x_{\circledast}$ as

$$k_{\circledast} = x_{\circledast} K_{\circledast} \, . \tag{2.1}$$

We choose our reference frame with the z axis along the $k_\oplus$ direction. We introduce the following variables

$$M^2 = (k_1 + k_2)^2, \qquad Y = \frac{1}{2} \log \frac{(k_1 + k_2)^0 + (k_1 + k_2)^3}{(k_1 + k_2)^0 - (k_1 + k_2)^3}, \tag{2.2}$$

that characterize the invariant mass and rapidity of the virtual vector boson.[2] We also introduce the angle θ_l that represents the angle between the outgoing lepton and the $k_\oplus$ momentum, in the centre-of-mass frame of the lepton pair. The azimuthal orientation of the decay products is irrelevant here, since the cross sections do not depend upon it. We thus fix it to zero. At the end of the generation of the event, we perform a uniform, random azimuthal rotation of the whole event, in order to cover all final-state phase space. The set of variables M^2, Y and θ_l fully parametrize our Born kinematics. From them we can reconstruct

$$x_\oplus = \sqrt{\frac{M^2}{S}} e^Y, \qquad x_\ominus = \sqrt{\frac{M^2}{S}} e^{-Y}, \tag{2.3}$$

[1] In case of W production the quark-antiquark and lepton-antilepton pairs have different flavour. We focus here for simplicity on leptonic decays of the vector bosons. Hadronic decays are treated similarly.

[2] The virtuality of the lepton pair M^2 will be distributed according to a Breit-Wigner formula around the squared mass of the vector boson M_V^2 (where V stands for either the $W^\pm$ or the Z).

JHEP07(2008)060

where $S = (K_\oplus + K_\ominus)^2$. The leptons' momenta are first reconstructed in the longitudinal rest frame of the lepton pair, where each lepton has energy equal to $M/2$ and where the lepton momentum forms an angle θ_l with the $\oplus$ direction and has zero azimuth (i.e. it lies in the z, x plane and has positive x component). The leptons' momenta are then boosted with boost angle Y.

The Born phase space in terms of these variables is written as

$$\begin{aligned} d\mathbf{\Phi}_2 &= dx_\oplus\, dx_\ominus (2\pi)^4 \delta^4(k_\oplus + k_\ominus - k_1 - k_2) \frac{d^3k_1}{(2\pi)^3 2k_1^0} \frac{d^3k_2}{(2\pi)^3 2k_2^0} \\ &= \frac{1}{S}\frac{1}{16\pi} dM^2\, dY\, d\cos\theta_l \frac{d\phi_l}{2\pi}\,. \end{aligned} \tag{2.4}$$

2.1.2 Real-emission kinematics

The real emission process is described by the final-state momenta k_1, k_2 and k_3, where k_1 and k_2 have the same meaning as before, and k_3 is the momentum of the radiated light parton. In the POWHEG framework, applied in the context of the CS subtraction method, one introduces a different real phase-space parametrization for each CS dipole. In the present case, we have two CS dipoles, with the two incoming partons playing the role of the emitter and the spectator. We consider the case of the $\oplus$ collinear direction. Thus, the emitter is the incoming parton with momentum $k_\oplus$. We introduce the variable

$$x = 1 - \frac{(k_\oplus + k_\ominus)\cdot k_3}{k_\oplus \cdot k_\ominus}, \tag{2.5}$$

and the momenta

$$K = k_1 + k_2 = k_\oplus + k_\ominus - k_3 \tag{2.6}$$

$$\bar{K} = x\, k_\oplus + k_\ominus\,. \tag{2.7}$$

Observe that $K^2 = \bar{K}^2$, which is the condition that fixes the value of x. When k_3 is collinear to $k_\oplus$ we have

$$x k_\oplus = k_\oplus - k_3, \tag{2.8}$$

and $K = \bar{K}$. Following ref. [6], we introduce the boost tensor

$$\Lambda^\mu{}_\nu(K, \bar{K}) = g^\mu{}_\nu - \frac{2(K+\bar{K})^\mu (K+\bar{K})_\nu}{(K+\bar{K})^2} + \frac{2\bar{K}^\mu K_\nu}{K^2}\,, \tag{2.9}$$

the barred momenta

$$\bar{k}_r^\mu = \Lambda^\mu{}_\nu(K, \bar{K})\, k_r^\nu \qquad\qquad r = 1, 2, \tag{2.10}$$

the barred-momentum fractions

$$\bar{x}_\oplus = x\, x_\oplus, \qquad\qquad \bar{x}_\ominus = x_\ominus\,, \tag{2.11}$$

and the barred incoming momenta

$$\bar{k}_\oplus = x k_\oplus = \bar{x}_\oplus K_\oplus, \qquad\qquad \bar{k}_\ominus = k_\ominus = \bar{x}_\ominus K_\ominus\,. \tag{2.12}$$

The barred momenta characterize the underlying-Born kinematics. We define then

$$\bar{M}^2 = (\bar{k}_1 + \bar{k}_2)^2 = (k_1 + k_2)^2, \qquad \bar{Y}_\oplus = \frac{1}{2} \log \frac{(\bar{k}_1 + \bar{k}_2)^0 + (\bar{k}_1 + \bar{k}_2)^3}{(\bar{k}_1 + \bar{k}_2)^0 - (\bar{k}_1 + \bar{k}_2)^3}, \tag{2.13}$$

and the angle $\bar{\theta}_l$ is defined as in the Born case, but in terms of the momenta $\bar{k}_\oplus$, $\bar{k}_\ominus$, $\bar{k}_1$ and $\bar{k}_2$.

The radiation variables are given by

$$x, \qquad v = \frac{k_\oplus \cdot k_3}{k_\oplus \cdot k_\ominus}, \qquad \phi, \tag{2.14}$$

where ϕ is the azimuth of k_3 around the z direction.

From the set of variables $\bar{M}^2$, $\bar{Y}_\oplus$, x, v and ϕ we can reconstruct the full production kinematics for the real-emission cross section. We summarize the reconstruction procedure from ref. [5]. From $\bar{M}^2$ and $\bar{Y}$ we reconstruct the barred momenta, as for the Born kinematics case. Then we reconstruct immediately

$$k_\oplus = \frac{\bar{k}_\oplus}{x}, \qquad k_\ominus = \bar{k}_\ominus, \tag{2.15}$$

and then

$$k_3 = v k_\ominus + (1 - x - v) k_\oplus + k_T, \tag{2.16}$$

where k_T has only transverse components. Its magnitude is determined by the on shell condition $k_3^2 = 0$, which yields

$$k_T^2 = 2 k_\oplus \cdot k_\ominus (1 - x - v) v \tag{2.17}$$

and its azimuth is ϕ. We then construct the vectors

$$K = k_\oplus + k_\ominus - k_3, \qquad \bar{K} = x k_\oplus + k_\ominus, \tag{2.18}$$

and the inverse boost

$$\Lambda^{-1}_{\mu\nu}(K, \bar{K}) = g_{\mu\nu} - \frac{2(K + \bar{K})_\mu (K + \bar{K})_\nu}{(K + \bar{K})^2} + \frac{2 K_\mu \bar{K}_\nu}{K^2}, \tag{2.19}$$

from which we can compute the leptons' momenta

$$k_r = \Lambda^{-1}(K, \bar{K})\, \bar{k}_r, \qquad r = 1, 2. \tag{2.20}$$

The real-emission phase space can be expressed in a factorized form in terms of the underlying Born kinematics phase space and of the radiation variables

$$d\mathbf{\Phi}_3 = d\bar{\mathbf{\Phi}}_2\, d\Phi_{\rm rad}, \tag{2.21}$$

with

$$d\Phi_{\rm rad} = \frac{\bar{M}^2}{16\pi^2} \frac{d\phi}{2\pi}\, dv\, \frac{dx}{x^2}\, \theta(v)\, \theta\left(1 - \frac{v}{1 - x}\right) \theta(x(1 - x))\, \theta(x - \bar{x}_\oplus) \tag{2.22}$$

JHEP07(2008)060

and

$$d\bar{\mathbf{\Phi}}_2 = \frac{1}{S}\,\frac{1}{16\pi}\,d\bar{M}^2\,d\bar{Y}\,d\cos\bar{\theta}_l\,. \tag{2.23}$$

The kinematic variables corresponding to the $\ominus$ collinear direction are reconstructed in full analogy. Observe that the underlying-Born variables and the radiation variables depend in general upon the collinear region that we are considering. In the present case, while $\bar{M}$, x and ϕ are obviously independent of the region we are considering, $\bar{Y}$, $\bar{\theta}_l$ and v do depend upon it. In order to avoid a too heavy notation, we have refrained from appending $\oplus$ or $\ominus$ indices to the underlying Born and radiation variables. When necessary, we will put a $[\ ]_{\circledast}$ "context" bracket around a formula, meaning that the underlying Born and radiation variables inside it should refer to the $\circledast$ direction.

2.2 Cross sections

We have used the helicity amplitude method of refs. [11, 12] in order to compute the cross sections including the vector-boson decay products, and checked our results with MadEvent [13]. For the W-boson propagator we have taken

$$\frac{-g_{\mu\nu} + q_\mu q_\nu/M_W^2}{q^2 - M_W^2 + i\Gamma_W M_W} \tag{2.24}$$

and for the Z/γ-boson propagators, multiplied by the corresponding couplings,

$$g_l\,g_q\,\frac{-g_{\mu\nu} + q_\mu q_\nu/M_Z^2}{q^2 - M_Z^2 + i\Gamma_Z M_Z} + e_l\,e_q\,\frac{-g_{\mu\nu}}{q^2}, \tag{2.25}$$

where g_l, g_q are the lepton and quark couplings to the Z (for given helicities), and e_l, e_q are their electric charges.

Following ref. [5], we introduce the Born $\mathcal{B}_{q\bar{q}}$ and the real-emission cross sections $\mathcal{R}_{q\bar{q},g}$, $\mathcal{R}_{g\bar{q},q}$ and $\mathcal{R}_{qg,\bar{q}}$, that represent the contributions for quark-antiquark, gluon-antiquark and quark-gluon initiating processes. Notice that the flavour of the outgoing particle in the subscript of $\mathcal{R}$ is also taken to be incoming. In the case of Z production, q and $\bar{q}$ are conjugate in flavour. For $W^\pm$ production, because of flavour mixing, q and $\bar{q}$ may refer to different flavour species. We thus assume that, in general, q and $\bar{q}$ may both represent any flavour, but, in general, if q is a quark, $\bar{q}$ is an antiquark, and viceversa. $\mathcal{B}$ and $\mathcal{R}$ are obtained by taking the absolute value squared of the corresponding helicity amplitude, summing over the helicities and colours of the outgoing particles, averaging over the helicities and colour of the initial partons, and multiplying by the flux factor $1/(2s)$ (see eq. (2.27)). The soft-virtual term in the CS approach is given by (see eq. (2.107) in ref. [5])

$$\mathcal{V}_{q\bar{q}} = \frac{\alpha_S}{\pi} C_F \mathcal{B}_{q\bar{q}}\,. \tag{2.26}$$

Defining

$$s = (k_\oplus + k_\ominus)^2, \qquad u = (k_\oplus - k_3)^2 = -s\,v, \qquad t = (k_\ominus - k_3)^2 = -(1-x-v)\,s, \tag{2.27}$$

the CS subtraction terms are given by

$$\mathcal{C}^{\oplus}_{q\bar{q},g} = \left[-\frac{1}{u}2\,g_s^2\,C_{\mathrm{F}}\left\{\frac{2}{1-x} - (1+x)\right\}\mathcal{B}_{q\bar{q}}(\bar{M},\bar{Y},\bar{\theta}_l)\right]_{\oplus}, \tag{2.28}$$

for gluon radiation from a $q\bar{q}$ initial-state, and

$$\mathcal{C}_{g\bar{q},q} = \left[-\frac{1}{u} 2\, g_s^2\, T_{\rm F} \left\{ 1 - 2\, x\, (1-x) \right\} \mathcal{B}_{q\bar{q}}(\bar{M}, \bar{Y}, \bar{\theta}_l) \right]_{\oplus} , \tag{2.29}$$

for the $g\bar{q}$. Analogous formulae apply for the $q\bar{q}$ and the qg counterterms in the $\ominus$ collinear direction.

The collinear remnants are given by

$$\begin{aligned} \mathcal{G}_{\oplus}^{q\bar{q},g}(\mathbf{\Phi}_{2,\oplus}) = \frac{\alpha_{\rm S}}{2\pi} C_{\rm F} \Bigg[& \left(\frac{2}{1-z} \log \frac{(1-z)^2}{z} \right)_+ - (1+z) \log \frac{(1-z)^2}{z} + (1-z) \\ & + \left(\frac{2}{3}\pi^2 - 5 \right) \delta(1-z) + \left(\frac{1+z^2}{1-z} \right)_+ \log \frac{M^2}{\mu_{\rm F}^2} \Bigg] \left[\mathcal{B}_{q\bar{q}}(\bar{M}, \bar{Y}, \bar{\theta}_l) \right]_{\oplus}, \end{aligned} \tag{2.30}$$

$$\mathcal{G}_{\oplus}^{g\bar{q},q}(\mathbf{\Phi}_{2,\oplus}) = \frac{\alpha_{\rm S}}{2\pi} T_{\rm F} \left\{ \left[z^2 + (1-z)^2 \right] \left[\log \frac{(1-z)^2}{z} + \log \frac{M^2}{\mu_{\rm F}^2} \right] + 2z(1-z) \right\} \left[\mathcal{B}_{q\bar{q}}(\bar{M}, \bar{Y}, \bar{\theta}_l) \right]_{\oplus}. \tag{2.31}$$

The $\mathbf{\Phi}_{2,\oplus}$ notation, according to ref. [5], represents the set of variables

$$\mathbf{\Phi}_{2,\oplus} = \{ x_\oplus, x_\ominus, z, k_1, k_2 \}, \qquad z\, x_\oplus K_\oplus + x_\ominus K_\ominus = k_1 + k_2 \,. \tag{2.32}$$

We also associate an underlying Born configuration $\bar{\mathbf{\Phi}}_2$ to the $\mathbf{\Phi}_{2,\oplus}$ kinematics, defined by

$$\bar{k}_\oplus = z\, x_\oplus K_\oplus, \qquad \bar{k}_\ominus = x_\ominus K_\ominus, \qquad \bar{k}_1 = k_1, \quad \bar{k}_2 = k_2 \,. \tag{2.33}$$

The other two collinear remnants, $\mathcal{G}_{\ominus}^{q\bar{q},g}(\mathbf{\Phi}_{2,\ominus})$ and $\mathcal{G}_{\ominus}^{qg,\bar{q}}(\mathbf{\Phi}_{2,\ominus})$, are equal to $\mathcal{G}_{\oplus}^{q\bar{q},g}(\mathbf{\Phi}_{2,\oplus})$ and $\mathcal{G}_{\oplus}^{g\bar{q},q}(\mathbf{\Phi}_{2,\oplus})$ respectively, with $\left[\mathcal{B}_{q\bar{q}}(\bar{M}, \bar{Y}, \bar{\theta}_l) \right]_{\oplus}$ replaced by $\left[\mathcal{B}_{q\bar{q}}(\bar{M}, \bar{Y}, \bar{\theta}_l) \right]_{\ominus}$. We then introduce the notation B, V, R, C, G, to stand for $\mathcal{B}$, $\mathcal{V}$, $\mathcal{R}$, $\mathcal{C}$, $\mathcal{G}$, each multiplied by its appropriate parton densities. The differential cross section, multiplied by some infrared safe observable O, can then be written as

$$\begin{aligned} \langle O \rangle = \sum_{q\bar{q}} \Bigg\{ & \int d\mathbf{\Phi}_2 \left[B_{q\bar{q}}(\mathbf{\Phi}_2) + V_{q\bar{q}}(\mathbf{\Phi}_2) \right] O(\mathbf{\Phi}_2) \\ & + \int d\mathbf{\Phi}_3 \left\{ R_{q\bar{q},g}(\mathbf{\Phi}_3) O(\mathbf{\Phi}_3) - C^{\oplus}_{q\bar{q},g}(\mathbf{\Phi}_3) \left[O(\bar{\mathbf{\Phi}}_2) \right]_{\oplus} - C^{\ominus}_{q\bar{q},g}(\mathbf{\Phi}_3) \left[O(\bar{\mathbf{\Phi}}_2) \right]_{\ominus} \right\} \\ & + \int d\mathbf{\Phi}_3 \left\{ R_{g\bar{q},q}(\mathbf{\Phi}_3) O(\mathbf{\Phi}_3) - C_{g\bar{q},q}(\mathbf{\Phi}_3) \left[O(\bar{\mathbf{\Phi}}_2) \right]_{\oplus} \right\} \\ & + \int d\mathbf{\Phi}_3 \left\{ R_{qg,\bar{q}}(\mathbf{\Phi}_3) O(\mathbf{\Phi}_3) - C_{qg,\bar{q}}(\mathbf{\Phi}_3) \left[O(\bar{\mathbf{\Phi}}_2) \right]_{\ominus} \right\} \\ & + \int d\mathbf{\Phi}_{2,\oplus} \left[G_{\oplus}^{q\bar{q},g}(\mathbf{\Phi}_{2,\oplus}) + G_{\oplus}^{g\bar{q},q}(\mathbf{\Phi}_{2,\oplus}) \right] O(\mathbf{\Phi}_{2,\oplus}) \\ & + \int d\mathbf{\Phi}_{2,\ominus} \left[G_{\ominus}^{q\bar{q},g}(\mathbf{\Phi}_{2,\ominus}) + G_{\ominus}^{qg,\bar{q}}(\mathbf{\Phi}_{2,\ominus}) \right] O(\mathbf{\Phi}_{2,\ominus}) \Bigg\} . \end{aligned} \tag{2.34}$$

JHEP07(2008)060

3. POWHEG implementation

The starting point of a POWHEG implementation is the inclusive cross section at fixed underlying-Born flavour and kinematics. For the soft-virtual and Born contributions the underlying Born kinematics is obviously given by the Born kinematics itself. For the collinear remnant, for example, in the $\oplus$ direction (see eq. 2.32) the underlying Born kinematics is given by

$$\bar{\mathbf{\Phi}}_2 = \{z x_\oplus, x_\ominus, k_1, k_2\}\,. \tag{3.1}$$

For the CS counterterms, the underlying Born kinematics is given by the corresponding $\bar{\mathbf{\Phi}}_2$ variables defined in eqs. (2.11) and (2.12). In order to assign an underlying Born kinematics to the real term, one has to decompose it into contributions that are singular in only one kinematic region. Since $R_{g\bar{q},q}$ and $R_{qg,\bar{q}}$ are only singular in the $\oplus$ and $\ominus$ direction respectively, we assign their underlying Born to be the same of the corresponding CS subtraction term. For $R_{q\bar{q},g}$, on the other hand, we separate:

$$R_{q\bar{q},g} = R^{\oplus}_{q\bar{q},g} + R^{\ominus}_{q\bar{q},g}, \qquad R^{\textcircled{\pm}}_{q\bar{q},g} = R_{q\bar{q},g}\frac{C^{\textcircled{\pm}}_{q\bar{q},g}}{C^{\oplus}_{q\bar{q},g} + C^{\ominus}_{q\bar{q},g}}\,, \tag{3.2}$$

and assign to $R^{\textcircled{\pm}}_{q\bar{q},g}$ the same underlying Born kinematics of the corresponding CS counterterm $C^{\textcircled{\pm}}_{q\bar{q},g}$. The underlying Born flavour, on the other hand, is always $q\bar{q}$ in the notation we have adopted.

3.1 Generation of the Born variables

The primary ingredient for a POWHEG implementation is the $\bar{B}$ function, that is the inclusive cross section at fixed underlying Born variables. In our case, it is given by

$$\bar{B} = \sum_{q\bar{q}} \bar{B}_{q\bar{q}}, \tag{3.3}$$

$$\begin{aligned}\bar{B}_{q\bar{q}} = {} & B_{q\bar{q}}(\mathbf{\Phi}_2) + V_{q\bar{q}}(\mathbf{\Phi}_2) + \sum_{\textcircled{\pm}} \int \left[d\Phi_{\rm rad}\left\{R^{\textcircled{\pm}}_{q\bar{q},g}(\mathbf{\Phi}_3) - C^{\textcircled{\pm}}_{q\bar{q},g}(\mathbf{\Phi}_3)\right\}\right]^{\bar{\mathbf{\Phi}}_2=\mathbf{\Phi}_2}_{\textcircled{\pm}} \\ & + \int \left[d\Phi_{\rm rad}\left\{R_{g\bar{q},q}(\mathbf{\Phi}_3) - C_{g\bar{q},q}(\mathbf{\Phi}_3)\right\}\right]^{\bar{\mathbf{\Phi}}_2=\mathbf{\Phi}_2}_{\oplus} + \int \left[d\Phi_{\rm rad}\left\{R_{qg,\bar{q}}(\mathbf{\Phi}_3) - C_{qg,\bar{q}}(\mathbf{\Phi}_3)\right\}\right]^{\bar{\mathbf{\Phi}}_2=\mathbf{\Phi}_2}_{\ominus} \\ & + \int_{\bar{x}_\oplus}^1 \frac{dz}{z}\left[G^{q\bar{q},g}_{\oplus}(\mathbf{\Phi}_{2,\oplus}) + G^{g\bar{q},q}_{\oplus}(\mathbf{\Phi}_{2,\oplus})\right]^{\bar{\mathbf{\Phi}}_2=\mathbf{\Phi}_2} + \int_{\bar{x}_\ominus}^1 \frac{dz}{z}\left[G^{q\bar{q},g}_{\ominus}(\mathbf{\Phi}_{2,\ominus}) + G^{qg,\bar{q}}_{\ominus}(\mathbf{\Phi}_{2,\ominus})\right]^{\bar{\mathbf{\Phi}}_2=\mathbf{\Phi}_2}\end{aligned} \tag{3.4}$$

The radiation variables $\Phi_{\rm rad}$ are parametrized in terms of three variables that span the unit cube, $X_{\rm rad} = \{X^{(1)}_{\rm rad}, X^{(2)}_{\rm rad}, X^{(3)}_{\rm rad}\}$, while the z variable is parametrized in term of a single variable $X^{(1)}_{\rm rad}$ that ranges between 0 and 1. We then define the $\tilde{B}$ function

$$\begin{aligned}\tilde{B}_{q\bar{q}} = {} & B_{q\bar{q}}(\mathbf{\Phi}_2) + V_{q\bar{q}}(\mathbf{\Phi}_2) + \sum_{\textcircled{\pm}} \left[\left|\frac{\partial\Phi_{\rm rad}}{\partial X_{\rm rad}}\right| \left\{R^{\textcircled{\pm}}_{q\bar{q},g}(\mathbf{\Phi}_3) - C^{\textcircled{\pm}}_{q\bar{q},g}(\mathbf{\Phi}_3)\right\}\right]^{\bar{\mathbf{\Phi}}_2=\mathbf{\Phi}_2}_{\textcircled{\pm}} \\ & + \left[\left|\frac{\partial\Phi_{\rm rad}}{\partial X_{\rm rad}}\right| \left\{R_{g\bar{q},q}(\mathbf{\Phi}_3) - C_{g\bar{q},q}(\mathbf{\Phi}_3)\right\}\right]^{\bar{\mathbf{\Phi}}_2=\mathbf{\Phi}_2}_{\oplus} + \left[\left|\frac{\partial\Phi_{\rm rad}}{\partial X_{\rm rad}}\right| \left\{R_{qg,\bar{q}}(\mathbf{\Phi}_3) - C_{qg,\bar{q}}(\mathbf{\Phi}_3)\right\}\right]^{\bar{\mathbf{\Phi}}_2=\mathbf{\Phi}_2}_{\ominus}\end{aligned}$$

JHEP07(2008)060

$$+\left[\frac{1}{z}\frac{\partial z}{\partial X^{(1)}_{\rm rad}}\left\{G^{q\bar{q},g}_{\oplus}(\mathbf{\Phi}_{2,\oplus})+G^{g\bar{q},q}_{\oplus}(\mathbf{\Phi}_{2,\oplus})\right\}\right]^{\bar{\mathbf{\Phi}}_2=\mathbf{\Phi}_2}_{\oplus}$$
$$+\left[\frac{1}{z}\frac{\partial z}{\partial X^{(1)}_{\rm rad}}\left\{G^{q\bar{q},g}_{\ominus}(\mathbf{\Phi}_{2,\ominus})+G^{qg,\bar{q}}_{\ominus}(\mathbf{\Phi}_{2,\ominus})\right\}\right]^{\bar{\mathbf{\Phi}}_2=\mathbf{\Phi}_2}_{\ominus}, \tag{3.5}$$

so that defining $\tilde{B}=\sum_{q\bar{q}}\tilde{B}_{q\bar{q}}$, we have

$$\bar{B}=\int d^3X_{\rm rad}\,\tilde{B}\,. \tag{3.6}$$

In practice, the $\tilde{B}$ function is integrated numerically over all $\mathbf{\Phi}_2, X_{\rm rad}$ integration variables, using an integration program that can generate the set of kinematic variables $\mathbf{\Phi}_2, X_{\rm rad}$, with a probability proportional to $d\mathbf{\Phi}_2\, d^3X_{\rm rad}\,\tilde{B}$ in the $d\mathbf{\Phi}_2\, d^3X_{\rm rad}$ kinematic cell (see, for example, refs. [14, 15]). Once the $\mathbf{\Phi}_2, X_{\rm rad}$ point is generated, the flavour $q\bar{q}$ is chosen with a probability proportional to the value of $\tilde{B}_{q\bar{q}}$ at that specific $\mathbf{\Phi}_2, X_{\rm rad}$ point. At this stage, the radiation variables are disregarded, and only the underlying Born ones are kept. This corresponds to integrate over the radiation variables.

3.2 Generation of the radiation variables

Radiation kinematics is instead generated using the POWHEG Sudakov form factor

$$\Delta^{q\bar{q}}(\mathbf{\Phi}_2,p_{\rm T})=\prod_{\circledast}\Delta^{q\bar{q}}_{\circledast}\,, \tag{3.7}$$

where

$$\Delta^{q\bar{q}}_{\oplus}(\mathbf{\Phi}_2,p_{\rm T})=\exp\left\{-\left[\int d\Phi_{\rm rad}\,\frac{R^{\oplus}_{q\bar{q},g}(\mathbf{\Phi}_3)+R_{g\bar{q},q}(\mathbf{\Phi}_3)}{B_{q\bar{q}}(\mathbf{\Phi}_2)}\,\theta\left(k_{\rm T}(\mathbf{\Phi}_3)-p_{\rm T}\right)\right]^{\bar{\mathbf{\Phi}}_2=\mathbf{\Phi}_2}_{\oplus}\right\} \tag{3.8}$$

$$\Delta^{q\bar{q}}_{\ominus}(\mathbf{\Phi}_2,p_{\rm T})=\exp\left\{-\left[\int d\Phi_{\rm rad}\,\frac{R^{\ominus}_{q\bar{q},g}(\mathbf{\Phi}_3)+R_{qg,\bar{q}}(\mathbf{\Phi}_3)}{B_{q\bar{q}}(\mathbf{\Phi}_2)}\,\theta\left(k_{\rm T}(\mathbf{\Phi}_3)-p_{\rm T}\right)\right]^{\bar{\mathbf{\Phi}}_2=\mathbf{\Phi}_2}_{\ominus}\right\} \tag{3.9}$$

The function $k_T(\mathbf{\Phi}_3)$ measures the hardness of radiation in the real event. It is required to be of the order of the transverse momentum of the radiation in the collinear limit, and to become equal to it in the soft-collinear limit. In principle, the choice of $k_T(\mathbf{\Phi}_3)$ can differ in the two singular regions ($\oplus$ and $\ominus$) that we are considering. The choice adopted in the Examples section of ref. [5] had in fact this feature. We have found, however, that for practical reasons[3] it is better to adopt a different choice, namely to take $k_T(\mathbf{\Phi}_3)$ to coincide with that of eqs. (2.16) and (2.17).

The generation of radiation is performed individually for $\Delta^{q\bar{q}}_{\oplus}$ and $\Delta^{q\bar{q}}_{\ominus}$, and the highest generated k_T is retained. The upper bounding function for the application of the veto

[3]The choice discussed in [5] is $k_T^2=M^2(1-x)v$, and is such that k_T^2 is always bound to be smaller than M^2. Since the factorization and renormalization scales are taken equal to k_T, for vector-boson production at transverse momenta much larger than the vector-boson mass the coupling does not properly decrease.

JHEP07(2008)060

method is chosen to be[4]

$$\frac{R^{\oplus}_{q\bar{q},g} + R_{g\bar{q},q}}{B_{q\bar{q}}} \leq \frac{16\pi^2}{M^2}\, N^{\oplus}_{q\bar{q}}\, \frac{\alpha_s(k_T^2)}{2v}\, \frac{x^2}{1-x-v}\,, \tag{3.10}$$

and the analogous one for the $\ominus$ direction. The procedure used to generate radiation events according to this upper bounding function is described in appendix A.

3.3 Born zeros

In case the Born cross section vanishes in particular kinematics points, a problem arises in the POWHEG expression for the Sudakov form factor (3.8) and (3.9). It happens, in fact, that although B vanishes, $\bar{B}$ may differ from zero. Born kinematics configurations with a vanishing Born cross section may thus be generated and, at the stage of radiation generation, one would find very large ratios of the real-emission cross section over the Born cross section. It would thus prove difficult to find a reasonable upper bound for this ratio. If one tries to neglect the problem, radiation events with a vanishing underlying Born configuration would never be generated. We observe that, in the limit of small hardness parameter, the real cross section also exhibits the same vanishing behaviour of the Born cross section. Loosely speaking, the problem arises when the distance of the underlying Born configuration from the zero configuration is smaller than the distance of the real emission cross section from the singular (i.e. zero hardness) configuration. In order to solve this problem, in a completely general way, we further decompose the real cross section contribution as (we use the notation of ref. [5])

$$R^{\alpha_r} = R^{\alpha_r,s} + R^{\alpha_r,r}, \tag{3.11}$$

where

$$R^{\alpha_r,s} = R^{\alpha_r}\,\frac{Z}{Z+H}, \qquad R^{\alpha_r,r} = R^{\alpha_r}\,\frac{H}{Z+H}. \tag{3.12}$$

The suffixes s and r stand for "singular" and "regular" respectively, and Z is a function of the kinematics that vanishes like the Born cross section, evaluated at the underlying Born kinematics of the given term. H is the hardness of radiation and it must vanish for vanishing transverse momentum of the radiation. The simplest possible choice would be

$$Z = \mathcal{B}\,\frac{k_{T,\max}^2}{\mathcal{B}_{\max}}, \qquad H = k_T^2\,, \tag{3.13}$$

where k_T is some definition of the transverse momentum of the radiation. Notice now that $R^{\alpha_r,s}$ vanishes as fast as the Born term when its underlying Born kinematics approaches the Born zero. It can thus be used in the expression for the Sudakov form factor (eqs. (3.8) and (3.9)) without problems. The $R^{\alpha_r,r}$ is instead non-vanishing, but, on the other hand, it does not have collinear or soft singularities because of the H factor, and thus it can be

[4]This upper bounding function differs from the ones of eqs. (7.163)–(7.166) in ref. [5], but is in fact equivalent to the bound of eq. (7.234) in the same reference, once the change of variables $\xi = 1-x$, $y = (1-2v-x)/(1-x)$ is performed, and the different definitions of $d\Phi_{\rm rad}$ are properly taken into account.

JHEP07(2008)060

computed directly, without any Sudakov form factor. In the case of W production, the Born zero is associated to $\bar{\theta}_l = 0$ if q is an antiquark, and $\bar{\theta}_l = \pi$ if it is a quark. We choose then

$$Z = M^2 \left(1 + s_q \cos\bar{\theta}_l\right)^2, \qquad H = k_T^2, \tag{3.14}$$

with k_T^2 given by formula (2.17) and the factor s_q equals 1 for quark, and -1 for antiquark. The angle $\bar{\theta}_l$ is chosen according to the $\oplus$ parametrization (for $R^{\oplus}$) or the $\ominus$ parametrization (for $R^{\ominus}$) of the real-emission phase space.

In addition, all the R^{α_r} terms in eq. (3.3) are replaced by the corresponding $R^{\alpha_r,s}$ and the $R^{\alpha_r,r}$ terms are generated in a way similar to what was done for eq. (3.5). In other words one defines

$$\begin{aligned}\tilde{B}^r = \sum_{q\bar{q}} \tilde{B}^r_{q\bar{q}} = \sum_{q\bar{q}} \Bigg\{ &\left[\left|\frac{\partial\Phi_{\rm rad}}{\partial X_{\rm rad}}\right| R^{\oplus,r}_{q\bar{q},g}(\mathbf{\Phi}_3)\right]_{\oplus}^{\bar{\mathbf{\Phi}}_2=\mathbf{\Phi}_2} + \left[\left|\frac{\partial\Phi_{\rm rad}}{\partial X_{\rm rad}}\right| R^{\ominus,r}_{q\bar{q},g}(\mathbf{\Phi}_3)\right]_{\ominus}^{\bar{\mathbf{\Phi}}_2=\mathbf{\Phi}_2} \\ &+ \left[\left|\frac{\partial\Phi_{\rm rad}}{\partial X_{\rm rad}}\right| R^{r}_{g\bar{q},q}(\mathbf{\Phi}_3)\right]_{\oplus}^{\bar{\mathbf{\Phi}}_2=\mathbf{\Phi}_2} + \left[\left|\frac{\partial\Phi_{\rm rad}}{\partial X_{\rm rad}}\right| R^{r}_{qg,\bar{q}}(\mathbf{\Phi}_3)\right]_{\ominus}^{\bar{\mathbf{\Phi}}_2=\mathbf{\Phi}_2} \Bigg\},\end{aligned} \tag{3.15}$$

and integrates over the whole $\mathbf{\Phi}_2, X_{\rm rad}$ phase space with the same method used for $\tilde{B}$. In order to generate an event, one chooses $\tilde{B}$ or $\tilde{B}^r$, with a probability proportional to their respective total integral. In case $\tilde{B}^r$ is chosen, one generates a kinematic configuration according to it. This kinematic configuration is a full 3-body configuration. The flavour $q\bar{q}$ is chosen with a probability proportional to the value of $\tilde{B}^r_{q\bar{q}}$ for the particular kinematic point that has been generated, and the event is sent to the output. In case $\tilde{B}$ is chosen, a kinematic configuration and an underlying Born flavour is chosen in the same way.

4. Results

The MC@NLO program provides an implementation of vector-boson production at the NLO level in a shower Monte Carlo framework. It should therefore be comparable to our calculation, and we thus begin by comparing MC@NLO and POWHEG distributions. In this comparison, the POWHEG code is interfaced to HERWIG [16, 17], in order to minimize differences due to the subsequent shower in the two approaches. We choose as our default parton-density functions the CTEQ6M [18] package, and the corresponding value of Λ_{QCD}. The factorization and renormalization scales are taken equal to $M_V^2 + (p_T^V)^2$ in the calculation of the $\bar{B}$ function, where $V = W$ or Z. In the generation of radiation, the factorization and renormalization scales are taken equal to the transverse momentum of the vector boson V. We also account properly for the heavy-flavour thresholds, when the transverse momentum of the vector boson approaches the bottom and charm quark threshold. That is to say, when the renormalization scale crosses a heavy-flavour mass threshold, the QCD evolution of the running coupling is accordingly changed to the new number of active flavours.

The other relevant parameters for our calculation are listed in table 1 and are used in eqs. (2.24) and (2.25). The W and Z couplings are given by

$$g = \frac{e}{\sin\theta_W^{\rm eff}}, \quad g_{l/q} = \frac{e}{\sin\theta_W^{\rm eff}\cos\theta_W^{\rm eff}}\left[T_3^{(l/q)} - q_{l/q}\sin^2\theta_W^{\rm eff}\right], \quad e = \sqrt{4\pi\alpha_{\rm em}(M_Z)}, \tag{4.1}$$

M_z (GeV)	Γ_Z (GeV)	M_W (GeV)	Γ_W (GeV)	$\sin^2\theta_W^{\rm eff}$	$\alpha_{\rm em}^{-1}(M_Z)$
91.188	2.49	80.419	2.124	0.23113	127.934

Table 1: Values of the physical parameters used throughout the paper.

ud	us	ub	cd	cs	cb	td	ts	tb
0.9748	0.2225	0.0036	0.2225	0.9740	0.041	0.009	0.0405	0.9992

Table 2: Absolute values of the CKM matrix elements used for W production.

where l/q denotes the given left or right component of a lepton or a quark. In table 2, we have collected the absolute values for the CKM matrix elements, used for W production. In all figures shown in the following we do not impose any acceptance cut.

4.1 Z production at the Tevatron

In figure 1 we show a comparison of the lepton transverse momentum and rapidity, and of the transverse momentum of the reconstructed lepton-antilepton pair at the Tevatron. We notice a larger cross section in POWHEG, when the Z transverse momentum becomes large. This is not unexpected, since for large momenta the POWHEG result is larger than the standard NLO result by a factor $\bar{B}/B$ (this feature has also some impact upon the transverse-momentum distribution of the lepton). Once this fact is accounted for, the transverse-momentum distribution of the Z is in fair agreement, although we find observable shape differences at low transverse momenta. We also notice a peak at $p_T = 0$ in the MC@NLO distribution, that is not present in the POWHEG result. We expect this distribution to be affected by low transverse-momentum power-suppressed effects. In fact, the peak at zero transverse momentum in MC@NLO disappears if the primordial transverse momentum of the partons (the PTRMS variable in HERWIG) is set to a non-zero value. In figure 2 we compare the rapidity distribution of the reconstructed Z, its invariant mass, the azimuthal distance of the e^+e^- pair coming from Z decays, and the transverse momentum of the radiated jet at the Tevatron. The jet is defined using the SISCONE algorithm [19] as implemented in the FASTJET package [20], using $R = 0.7$. We find again fair agreement.

In ref. [21], a discrepancy was found in the rapidity distribution of the hardest radiated jet as computed in MC@NLO and ALPGEN, for the case of top pair production at the Tevatron. The MC@NLO calculation shows there a dip at zero rapidity, not present in ALPGEN. In fact, the POWHEG calculation of this quantity does not display any dip. We thus examine the transverse momentum of the radiated jet in this case. Furthermore, we also plot the rapidity difference between the Z and the hardest radiated jet. The results are displayed in figure 3. We have chosen different cuts for the minimum transverse momentum of the radiated jet, i.e. 10, 20, 40, 60 and 80 GeV. We observe noticeable differences in the rapidity distribution of the hardest jet in the two approaches. The MC@NLO result displays a dip at zero $y_{\rm jet} - y_Z$.

4.2 Z production at the LHC

Similar results are reported for the LHC in figure 4 through 6.

JHEP07(2008)060

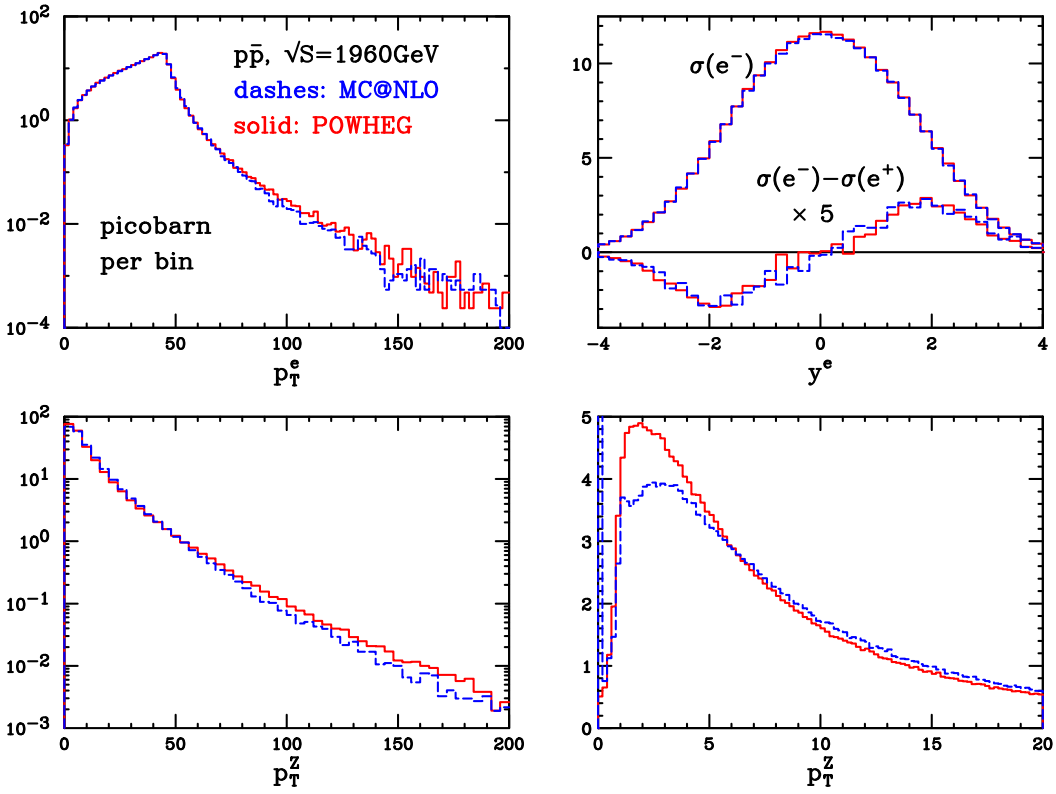

Figure 1: Comparison between POWHEG and MC@NLO results for the transverse momentum and rapidity of the lepton coming from the decay of the Z boson, and for the transverse momentum of the Z, as reconstructed from its decay products. The lepton-rapidity asymmetry is also shown. Plots done for the Tevatron $p\bar{p}$ collider.

We notice less pronounced differences (with respect to the Tevatron case) in the p_T spectrum of the Z boson. The discrepancy in the $y_{\rm jet}$ distribution is still evident, although the dip is barely noticeable in this case.

The same set of plots are also shown for a PYTHIA-POWHEG comparison in figure 7 through 10. In this case the POWHEG code was interfaced with PYTHIA. Photon radiation from final-state leptons was switched off (MSTJ(41)=3), in order to simplify the analysis. Furthermore, the new transverse-momentum ordered shower was used (i.e. the PYEVNW routine), since transverse-momentum ordering should be more appropriate in conjunction with POWHEG. In the plots, the PYTHIA output is normalized to the POWHEG total cross section. From figure 7 through 8, we can see a remarkable agreement between the two calculations for the Tevatron results, the only visible discrepancy being given by the transverse-momentum distribution of the Z boson at small transverse momenta. We also notice that, unlike the case of the MC@NLO-POWHEG comparison, the transverse-momentum distribution of the Z is slightly harder in PYTHIA than in POWHEG. The rapidity distributions of the hardest jet are also in remarkable agreement.

In figure 10 through 11, we carry out the same comparison in the LHC case. We notice here few important differences in the rapidity distribution of the Z boson, and, probably related to that, of the electron, the PYTHIA distribution being flatter in the central region.

JHEP07(2008)060

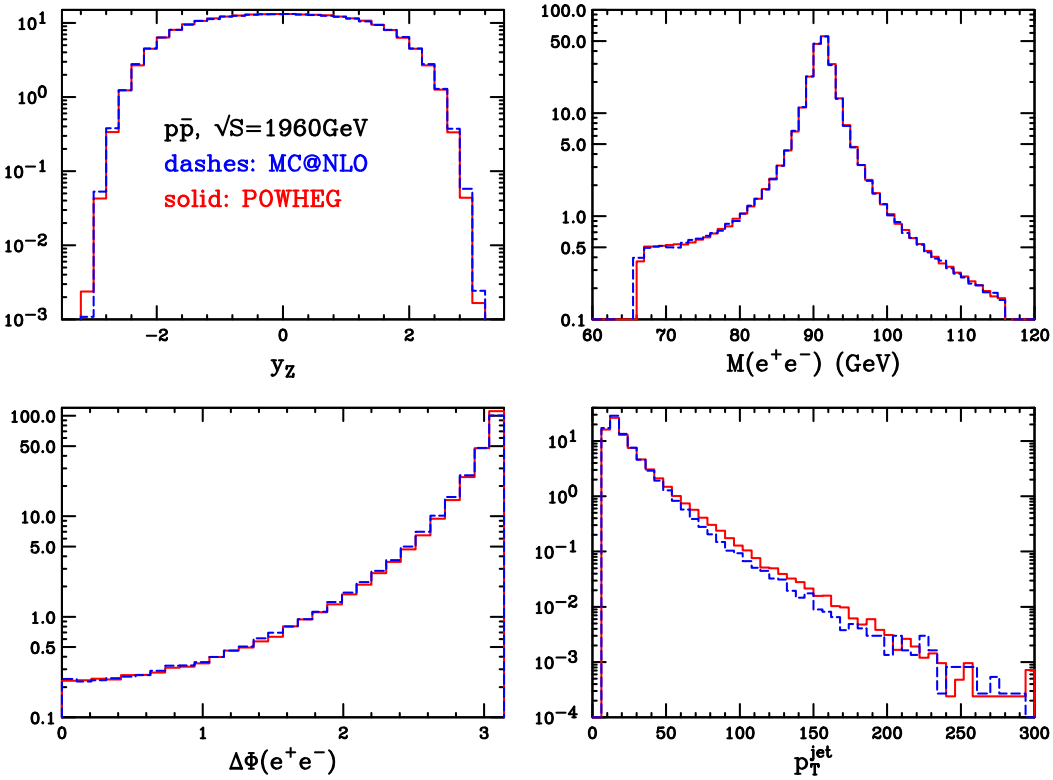

Figure 2: Comparison between POWHEG and MC@NLO for the reconstructed Z rapidity, its invariant mass, the lepton-pair azimuthal distance and the transverse momentum of the reconstructed jet, above a 10 GeV minimum value.

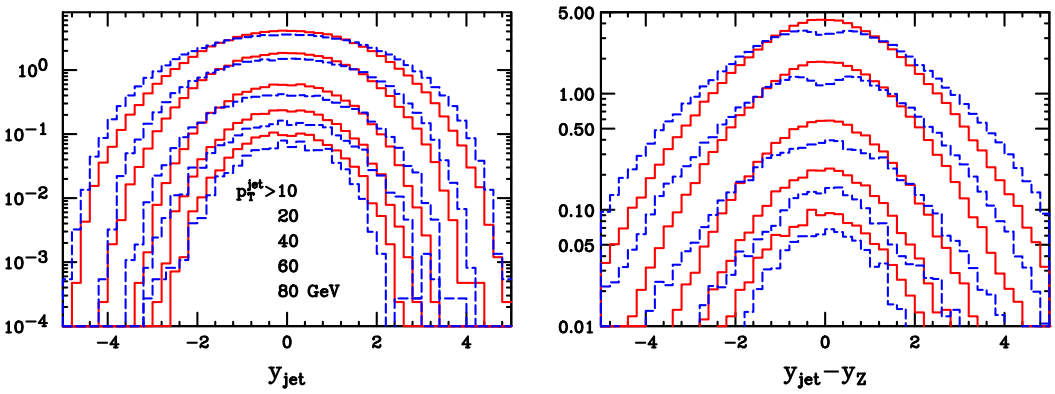

Figure 3: Rapidity distribution of the hardest jet with different transverse-momentum cuts, and the rapidity distance between the hardest jet and the reconstructed Z boson.

Both MC@NLO and POWHEG do not show this feature. As already pointed out in ref. [5], the generation of vector bosons in PYTHIA is not very different from the POWHEG generation. Radiation is generated with a very similar method [22, 23]. There are however differences. In PYTHIA the Born inclusive cross section is used rather than our $\bar{B}$ function. Furthermore, our choice of scales is constrained by the requirement of next-to-leading logarithmic accuracy in the Sudakov form factor. The discrepancy in the transverse-momentum dis-

JHEP07(2008)060

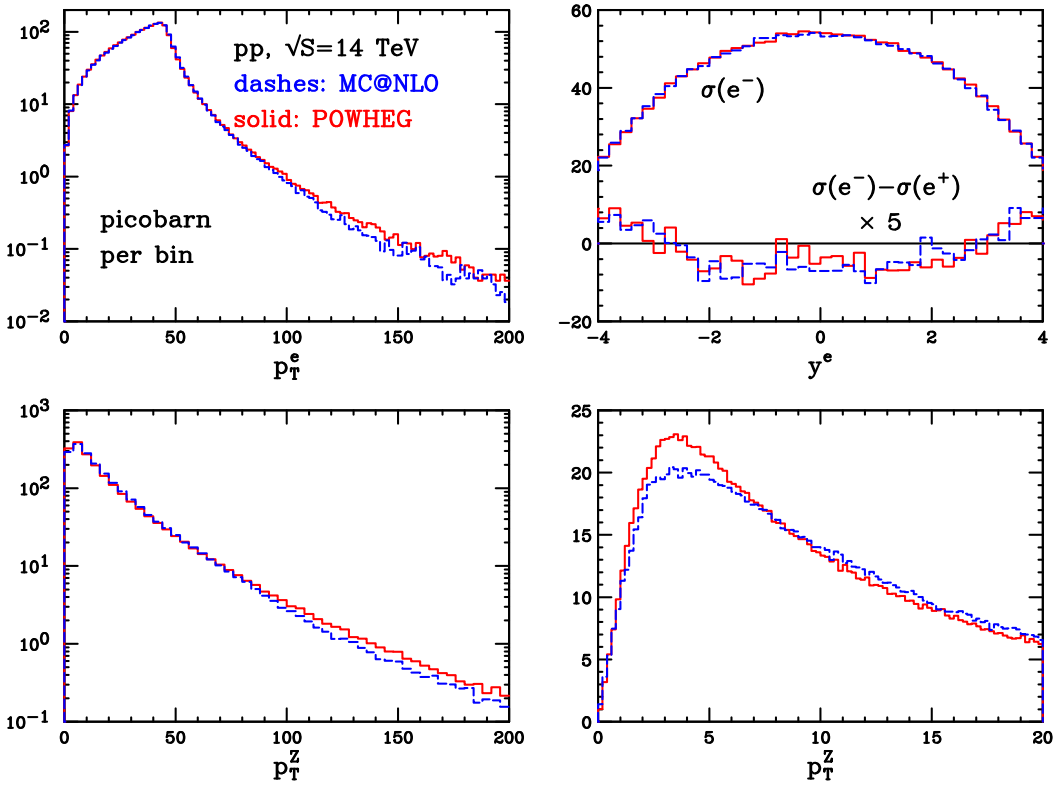

Figure 4: Same as figure 1 for the LHC at 14 TeV.

tribution of the Z may be due to different requirements for the choice of the scale in the generation of radiation in the two algorithms. The discrepancy in the rapidity distribution may be due to the lack of NLO corrections in PYTHIA, i.e. to the use of the Born cross section (rather than the $\bar{B}$ function) and LO parton densities. In fact, in figure 3 of ref. [24], a comparison in the rapidity distribution of the Z at LO, NLO and NNLO, is shown for the LHC. One can notice from that figure that there is a difference in the LO and NLO shape of the distribution, the former being flatter. In order to elucidate this point, we show in figure 13 the rapidity distribution of the Z boson computed at fixed order in QCD, at LO and NLO. With the LO calculation, we also show the result obtained using the same LO parton-distribution function (pdf) set used in PYTHIA, that is CTEQ5L. The figure leads to the conclusion that the use of the LO parton-density set CTEQ5L is the primary cause of this shape difference. We find, in fact, no difference in shape between the LO and NLO result if the same pdf set is used instead. We thus conclude that also the effect observed in figure 3 of ref. [24] is due to the use of a LO parton-density set together with the LO result.[5]

The predictions for the transverse-momentum distribution of the Z boson are summarized in figure 14, in comparison with data from ref. [25], at $\sqrt{S} = 1960\,\text{GeV}$ and from refs. [26 – 28] at $\sqrt{S} = 1800\,\text{GeV}$. The POWHEG+HERWIG and the MC@NLO output are obtained with an intrinsic transverse momentum of the incoming partons equal to 2.5 GeV (HERWIG's

[5]Some authors do prefer to use LO parton-density functions in LO calculations, although, in our opinion, there are no compelling reasons to do so.

JHEP07(2008)060

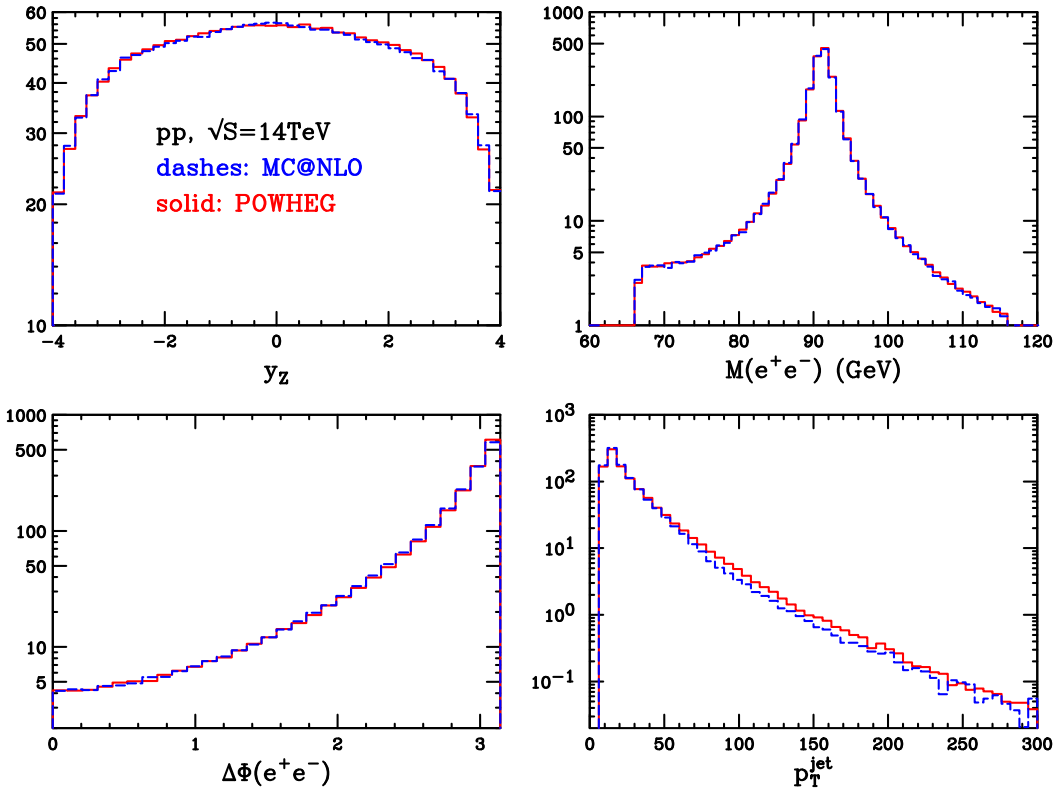

Figure 5: Same as figure 2 for the LHC at 14 TeV.

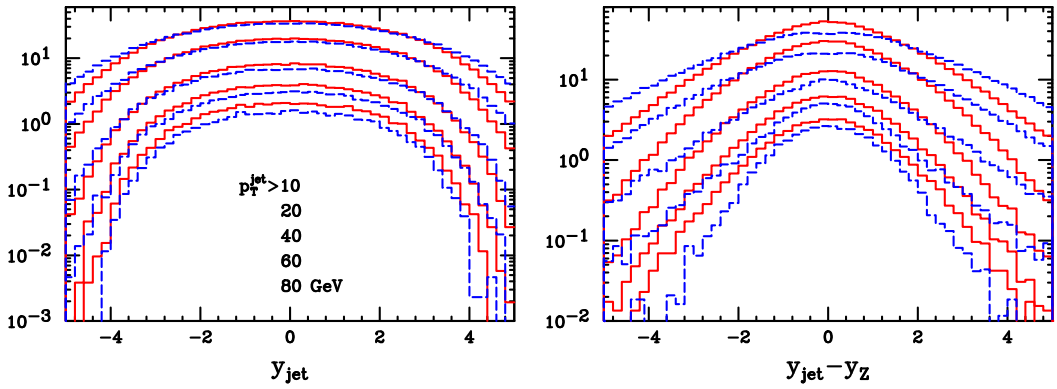

Figure 6: Same as figure 3 at the LHC at 14 TeV.

PTRMS parameter). Both data and predictions are normalized to 1. The difference in the shape of the distributions at 1960 and 1800 GeV are only minimal. We see that POWHEG with PYTHIA is in remarkable agreement with the MC@NLO result. On the other hand, standalone PYTHIA is closer to the output of POWHEG with HERWIG. In all cases, the agreement with data is not optimal. It is thus clear that this distribution is sensitive to long distance effects like hadronization and transverse-momentum smearing, and good agreement with data may only achieved by suitable tuning of the non-perturbative parameters of the shower Monte Carlo.

JHEP07(2008)060

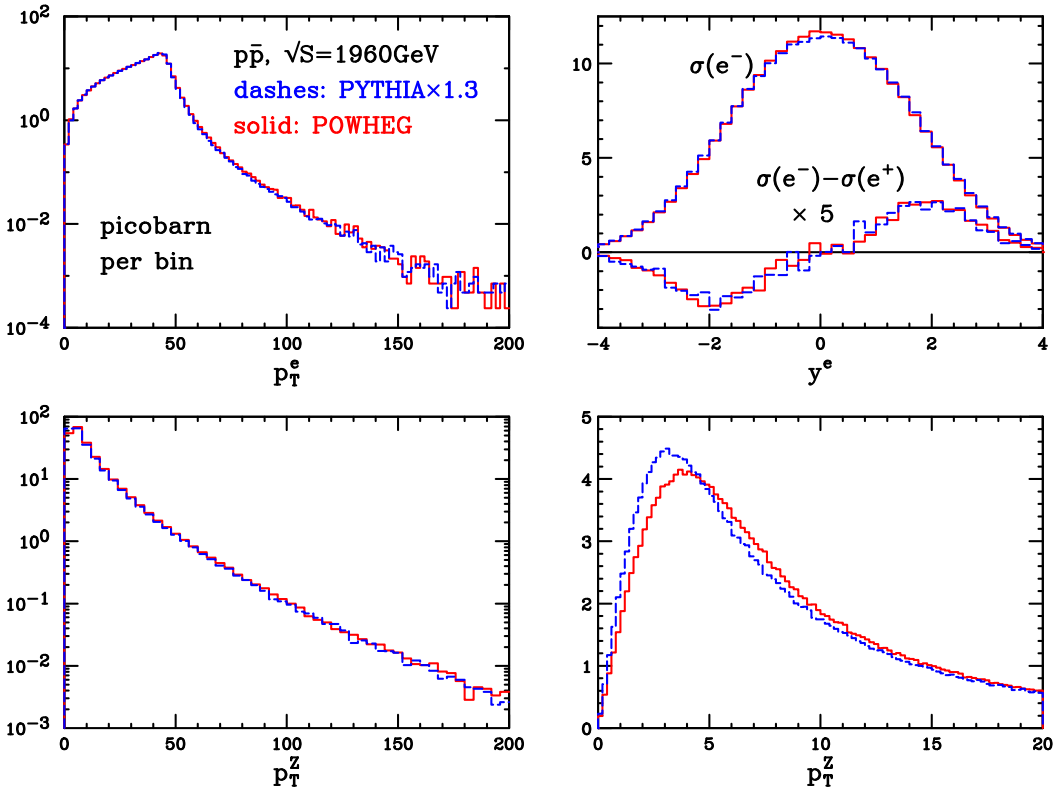

Figure 7: Same as figure 1 for a PYTHIA and POWHEG comparison at the Tevatron.

4.3 Hardest-jet rapidity distribution

The discrepancy of POWHEG and MC@NLO in the rapidity distribution of the hardest jet deserves further discussion.[6] In ref. [21], only the rapidity distribution of the hardest jet in $t\bar{t}$ production was considered, and a dip was found there, in the case of top-pair production at Tevatron energies. In the present case we found no dip in the rapidity distribution of the hardest jet in V production (see figure 3). We found instead a dip in the distribution in the rapidity difference between the jet and the vector boson. It is reasonable to assume that a dip in the rapidity distribution of the jet may be inherited from the dip in the rapidity difference, if the kinematics production regime is forced to be central, like in the case of top-pair production at the Tevatron. We thus also reconsider Z pair production and $t\bar{t}$ production at the Tevatron, and compare POWHEG and MC@NLO results for the rapidity distribution of the hardest jet, and for the distribution in the rapidity difference. The results are shown in figures 15 and 16.

From figure 15 we see that the dip present in the $y_{\rm jet} - y_{t\bar{t}}$ distribution is even deeper than the dip observed in the $y_{\rm jet}$ distribution. Furthermore, in figure 16, we see no particular features in the $y_{\rm jet}$ distribution. The $y_{\rm jet} - y_{\rm ZZ}$ distribution displays instead a tiny tower and a dip, depending upon the transverse-momentum cut on the jet. A deeper study of

[6] The distribution in the pseudorapidity difference of the hardest jet with respect to the vector boson was considered in ref. [29], in the context of a comparison of several matrix-element programs. Although noticeable differences are found among the generators considered there, none of them exhibit a dip at zero pseudorapidity.

JHEP07(2008)060

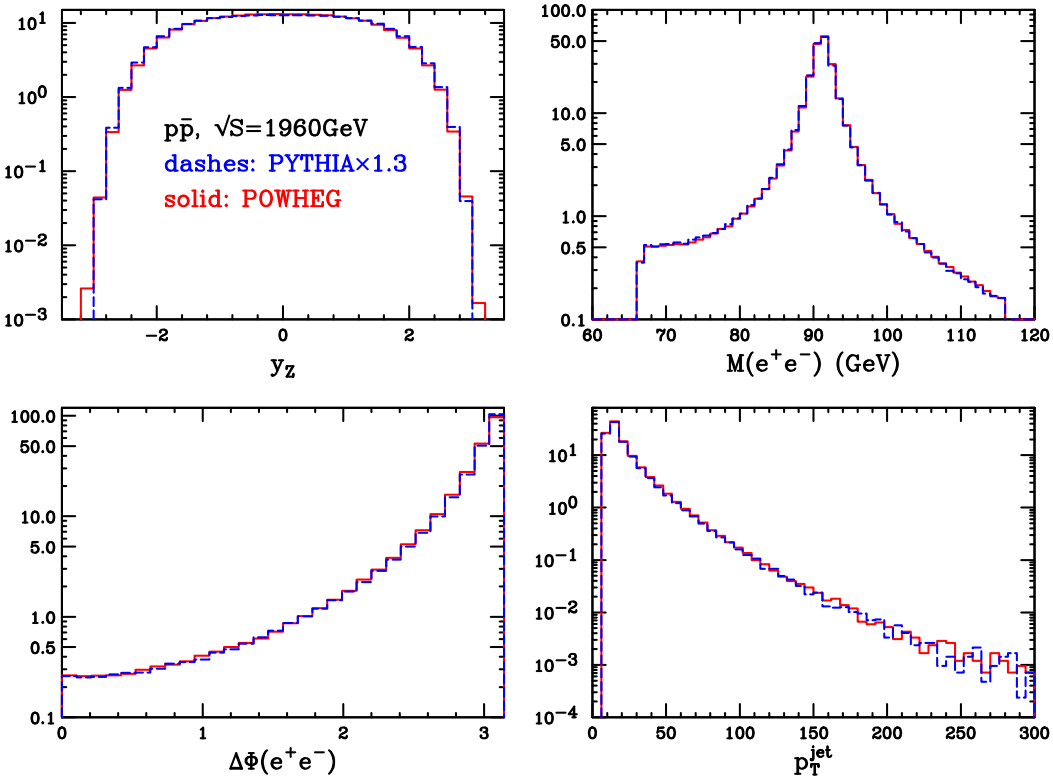

Figure 8: Same as figure 2 for a PYTHIA and POWHEG comparison at the Tevatron.

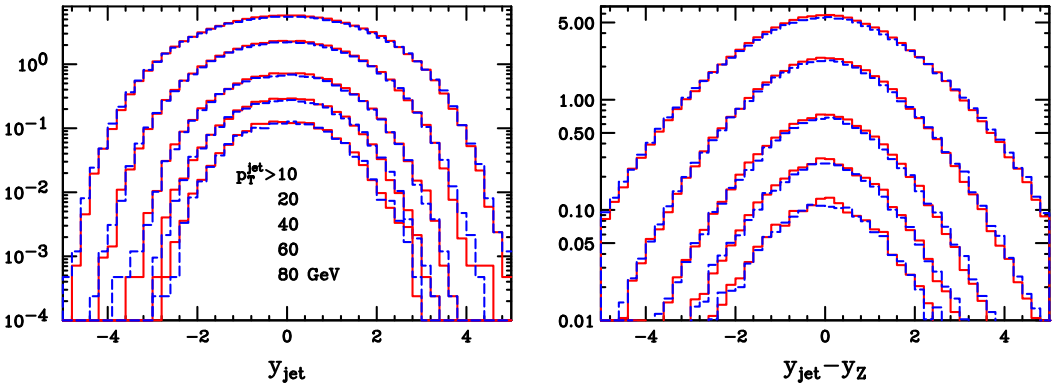

Figure 9: Same as figure 3 for a PYTHIA and POWHEG comparison at the Tevatron.

these features was performed in ref. [21], for $t\bar{t}$ production. It was shown there that the HERWIG Monte Carlo displays an even stronger dip than MC@NLO. The MC@NLO generator provides more events that partially fill the dip, thus correcting the NLO inaccuracies of the shower Monte Carlo. It is presumably a NNLO (next-to-next-to leading) mismatch between the twos that generates these features. On the other hand, the POWHEG program, as well as matrix-element generators, generate themselves the full NLO result, and thus are not sensitive to this feature of HERWIG. We also stress that these features do not mean that HERWIG is inaccurate at the LO level, or that MC@NLO is inaccurate at the NLO. A shower Monte Carlo is accurate in the radiation of the hardest jet only in the collinear regions.

JHEP07(2008)060

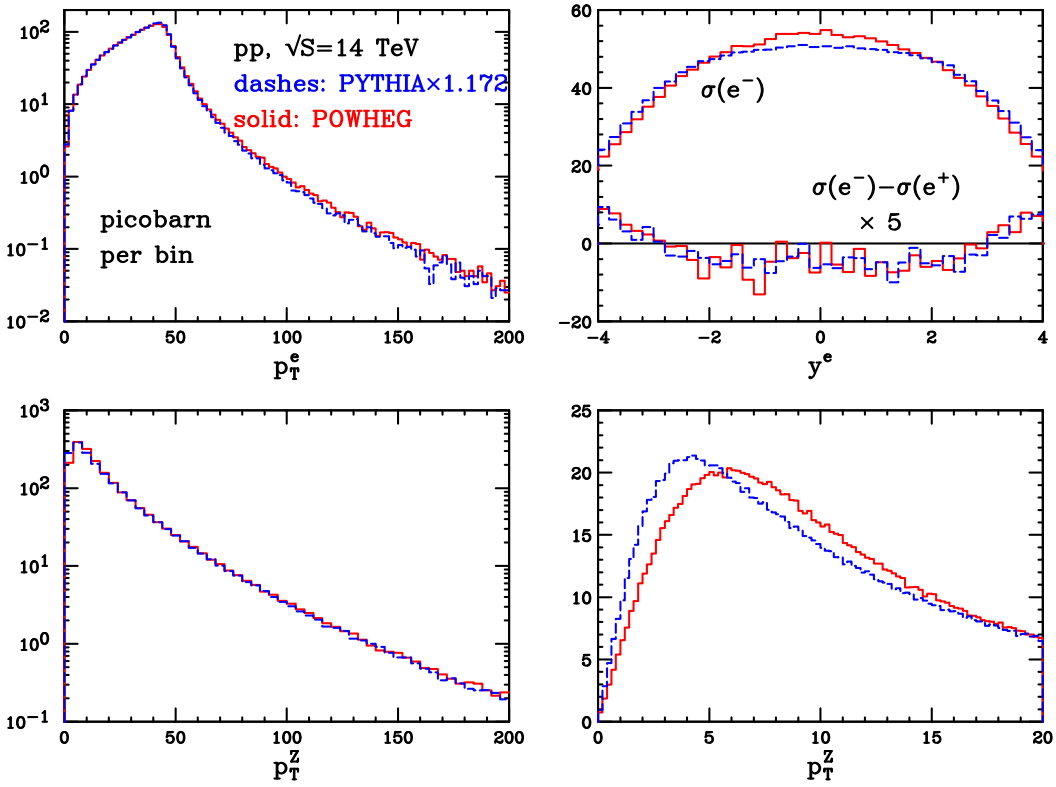

Figure 10: Same as figure 1 for a PYTHIA and POWHEG comparison at the LHC.

Furthermore, the dip in the MC@NLO result is compatible with an effect beyond NLO.

4.4 W production at the Tevatron and LHC

All results presented so far are relative to Z boson production. In the case of W production we find similar features and the comparison between MC@NLO and PYTHIA presents very similar characteristics. For the sake of completeness, we present in figure 17 through 34 plots of observables for W^- production at the Tevatron, and W^- and W^+ production at the LHC, comparing again the POWHEG output with MC@NLO and PYTHIA, and the observables for W^+ production at the LHC. We find again that MC@NLO displays dips in the rapidity distribution of the hardest jet at Tevatron energy. The comparison of the transverse-momentum distribution of the W shows the same differences found in the Z case. Furthermore, the rapidity distribution of the $W^\pm$ at the LHC differs in PYTHIA, showing a very marked difference in the W^+ case (see figure 33), probably (as in the Z case) a consequence of the different pdf set.

JHEP07(2008)060

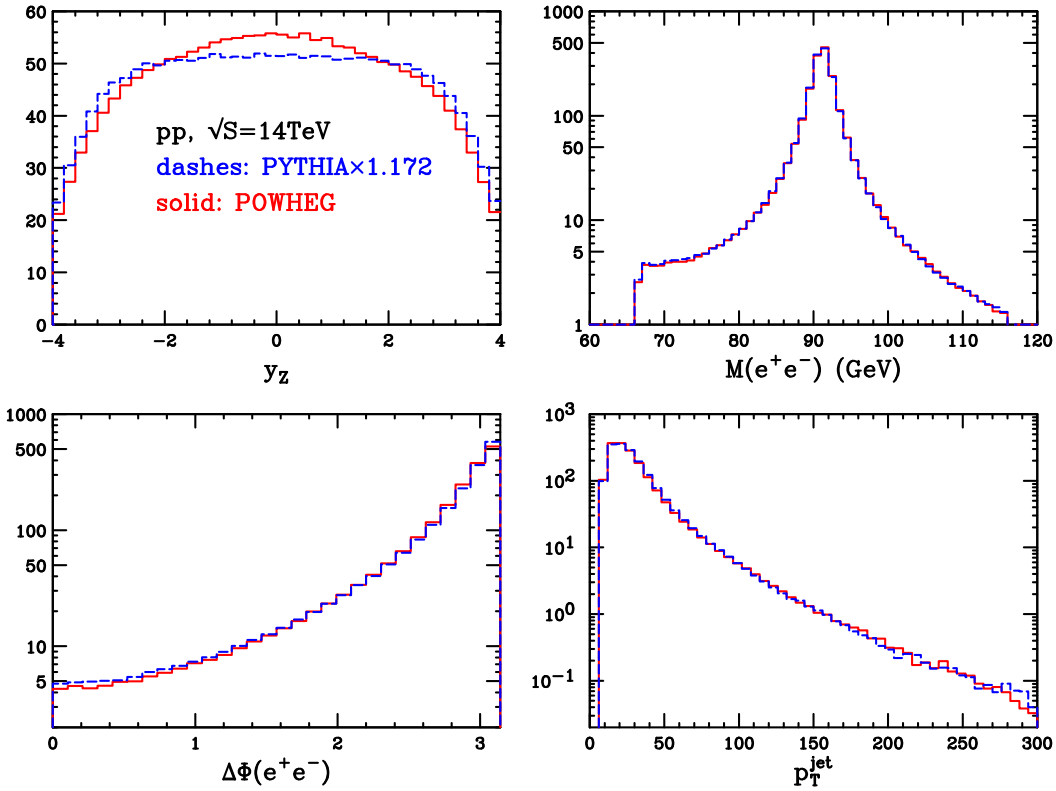

Figure 11: Same as figure 2 for a PYTHIA and POWHEG comparison at the LHC.

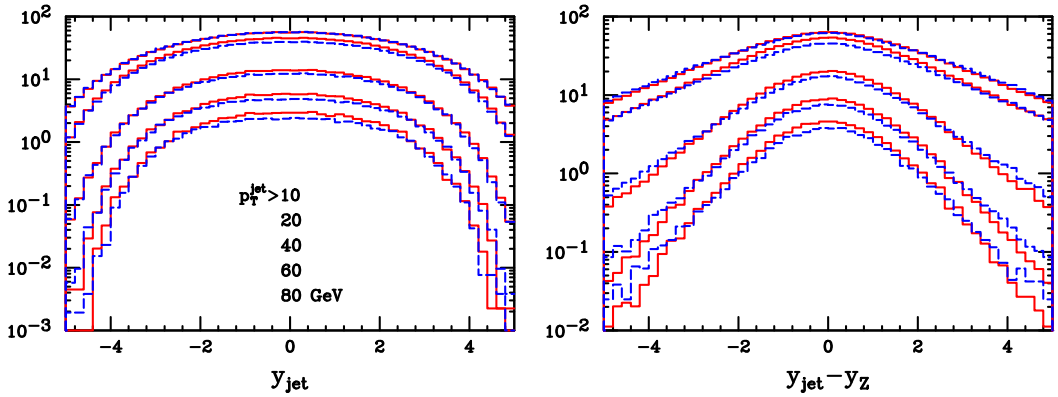

Figure 12: Same as figure 3 for a PYTHIA and POWHEG comparison at the LHC.

JHEP07(2008)060

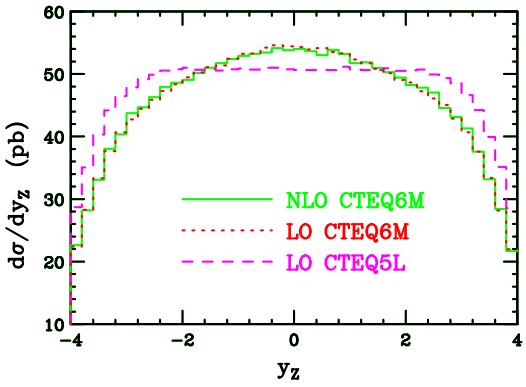

Figure 13: Rapidity distribution for the Z boson, computed at fixed order at LO and NLO. For the LO result, both the CTEQ6M and the CTEQ5L parton-density set were used. The plots are normalized to the NLO total cross section.

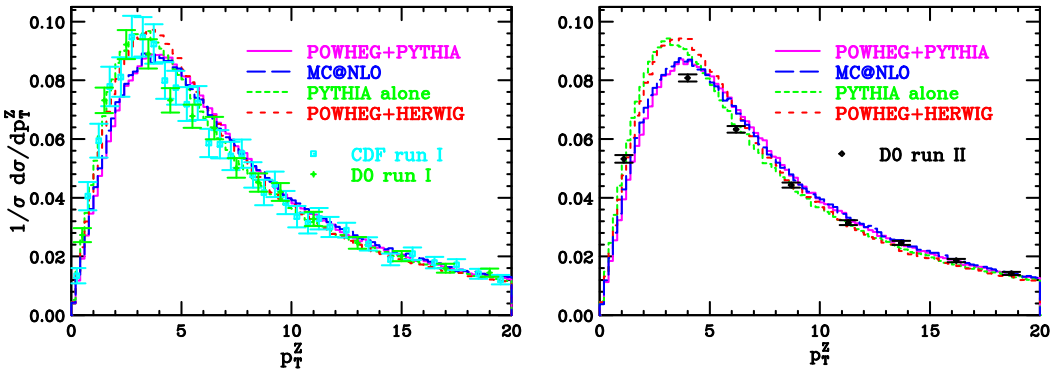

Figure 14: Comparison of transverse-momentum distributions of the Z bosons with data from the Tevatron.

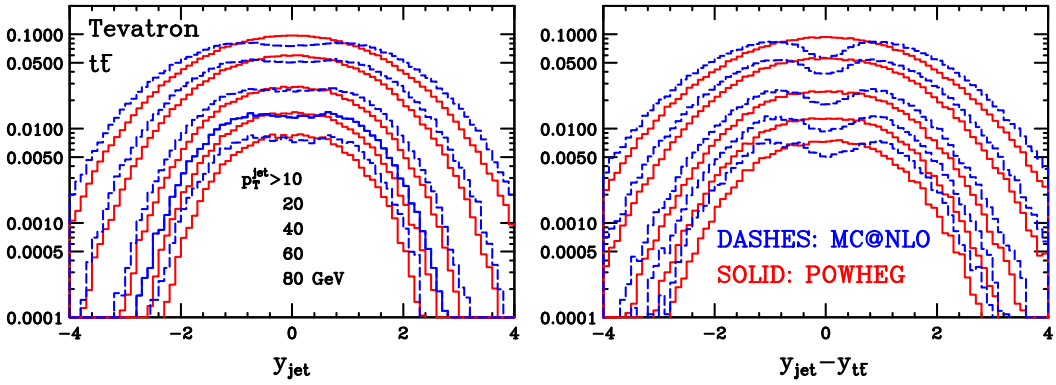

Figure 15: Rapidity distribution of the hardest jet and of the rapidity difference between the hardest jet and the $t\bar{t}$ system at Tevatron energies.

JHEP07(2008)060

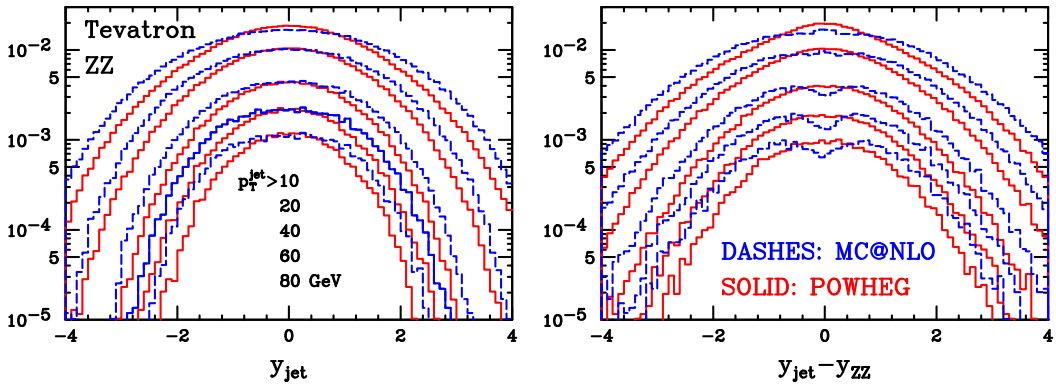

Figure 16: Rapidity distribution of the hardest jet and of the rapidity difference between the hardest jet and the ZZ system at Tevatron energies.

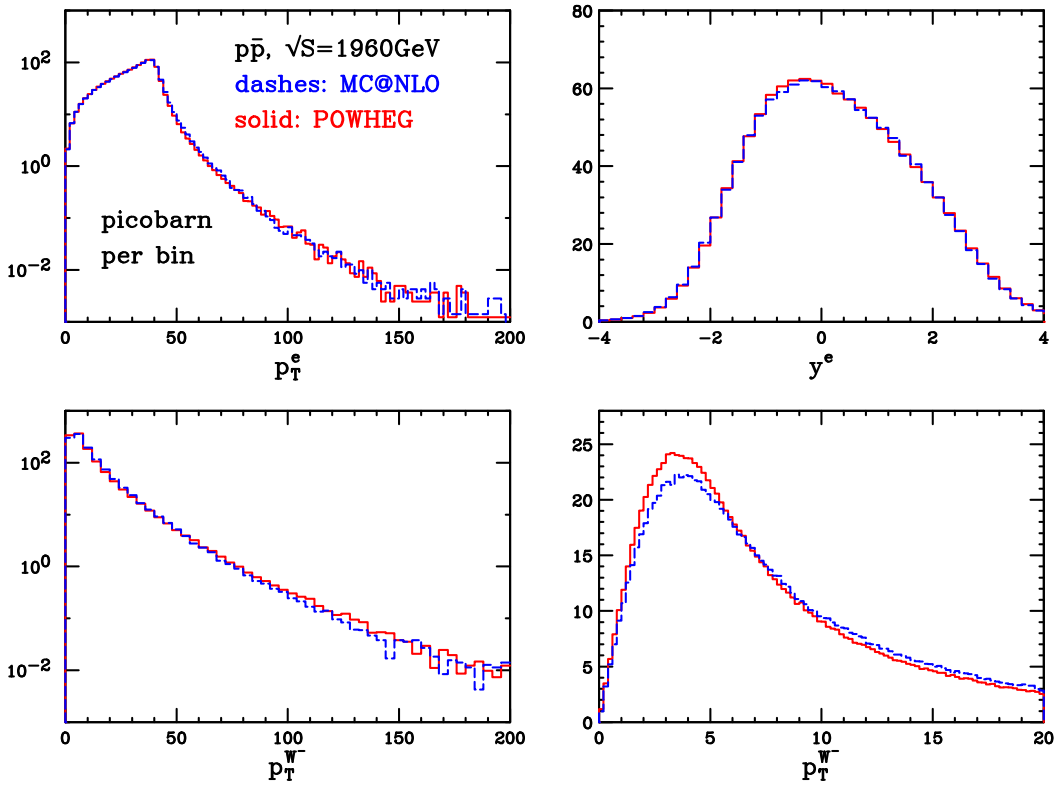

Figure 17: Comparison of POWHEG and MC@NLO results for the transverse momentum and rapidity of the lepton coming from the decay of the W^- boson and for the transverse momentum of the W^-, as reconstructed from its decay product.

JHEP07(2008)060

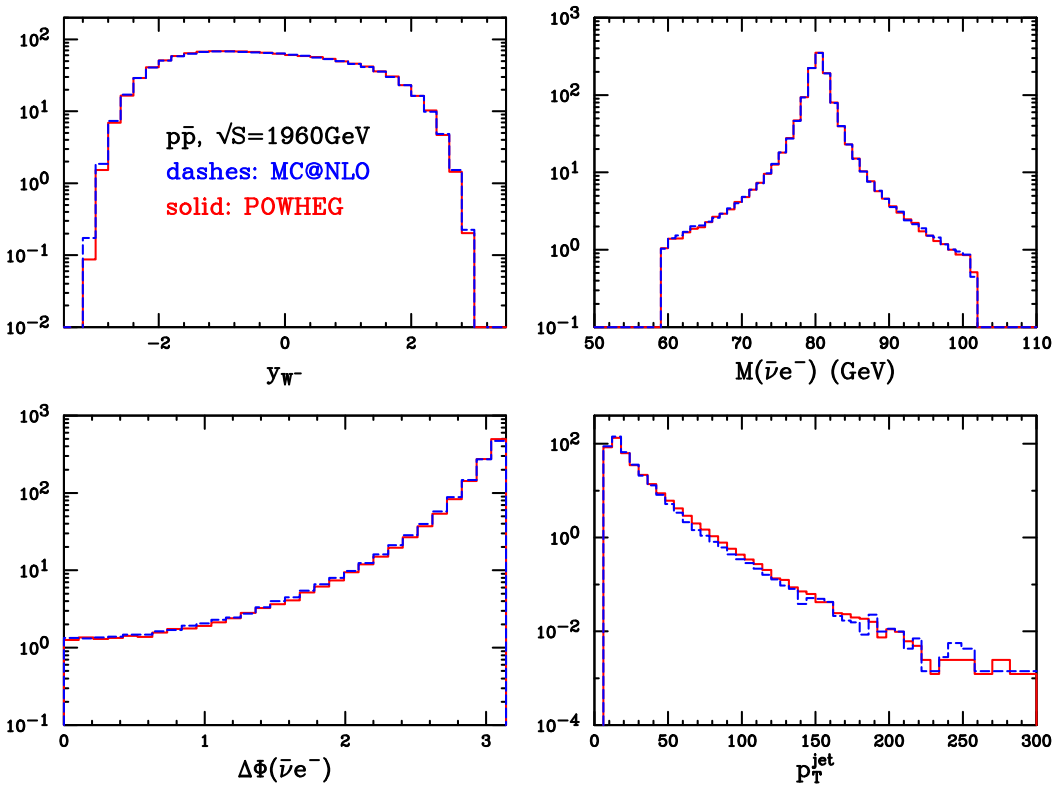

Figure 18: Comparison of POWHEG and MC@NLO for the reconstructed W^- rapidity, its invariant mass, the lepton-pair azimuthal distance and the transverse momentum of the reconstructed jet, above a 10 GeV minimum value.

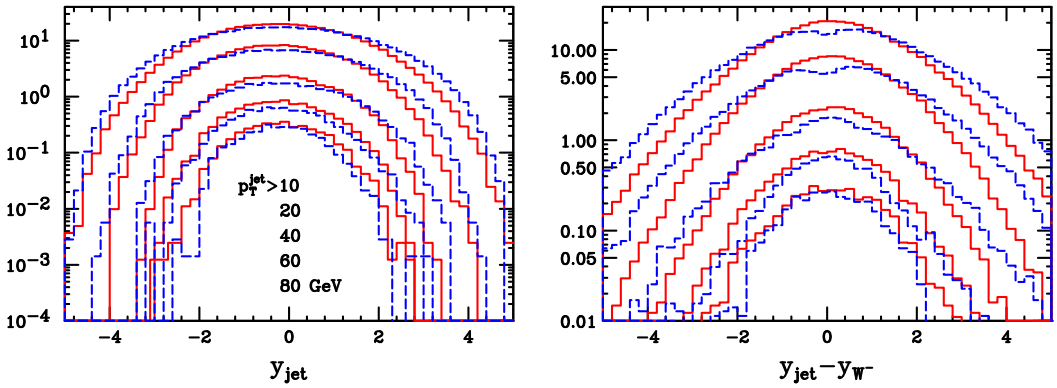

Figure 19: Rapidity distribution of the hardest jet with different transverse-momentum cuts, and the rapidity distance between the hardest jet and the reconstructed W^- boson for POWHEG and MC@NLO at the Tevatron.

JHEP07(2008)060

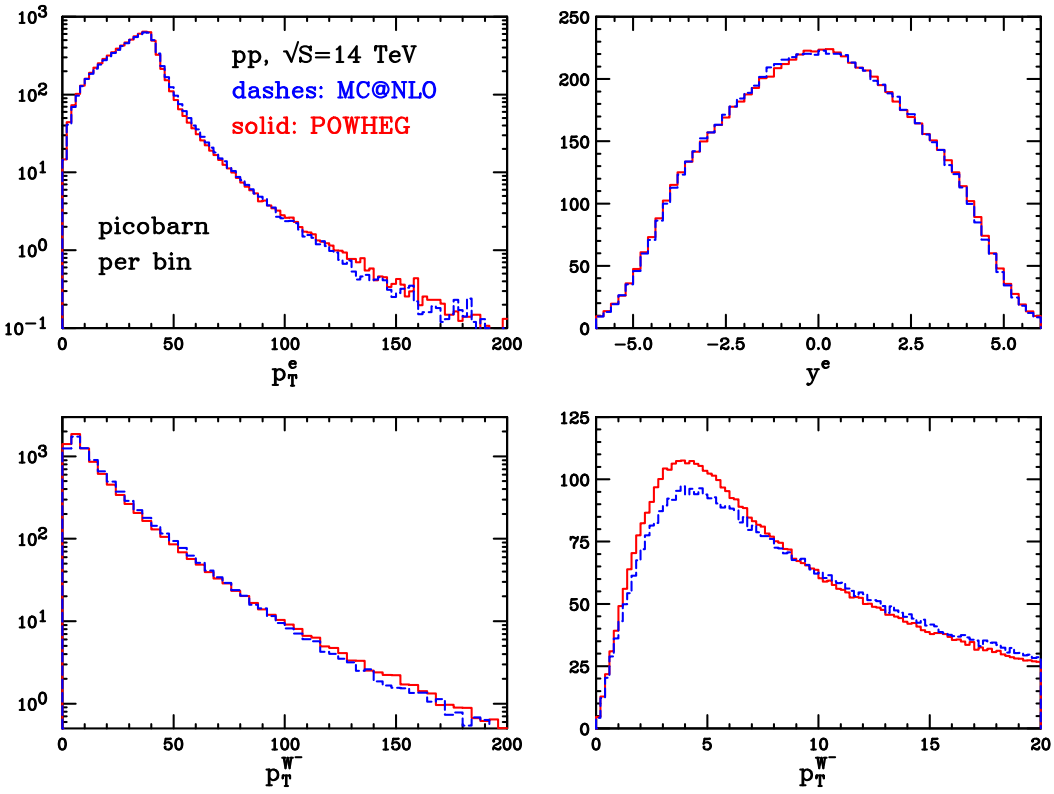

Figure 20: Same as figure 17 for the LHC at 14 TeV.

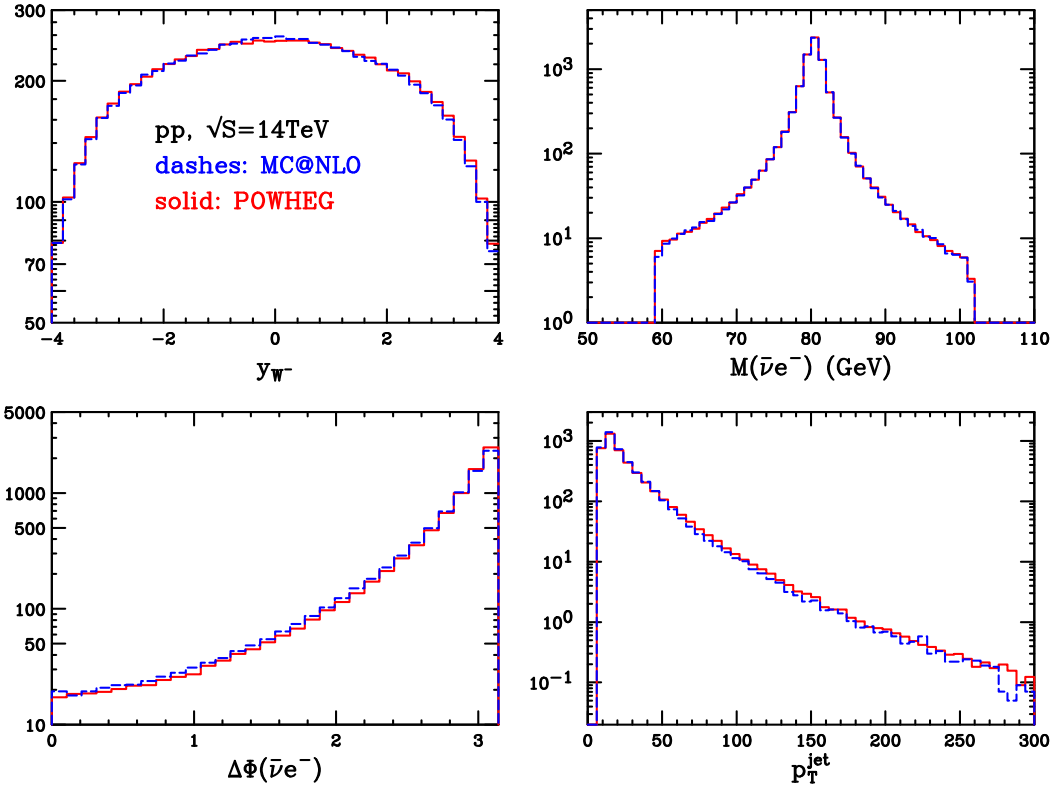

Figure 21: Same as figure 18 for the LHC at 14 TeV.

JHEP07(2008)060

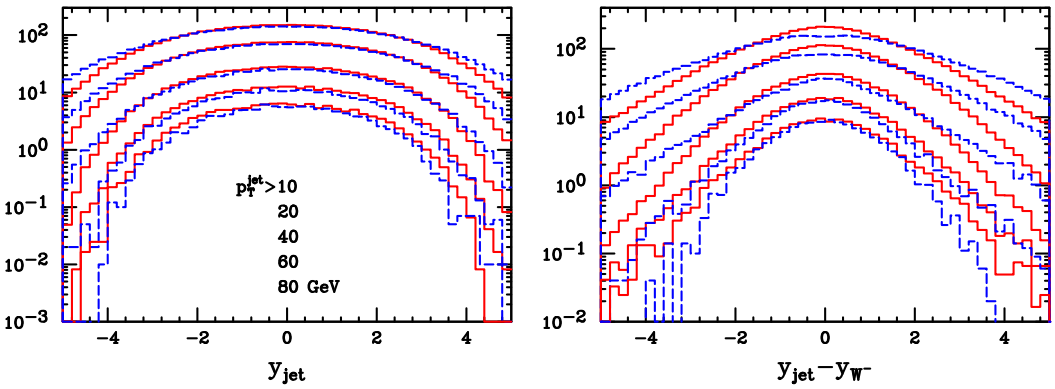

Figure 22: Same as figure 19 at the LHC at 14 TeV.

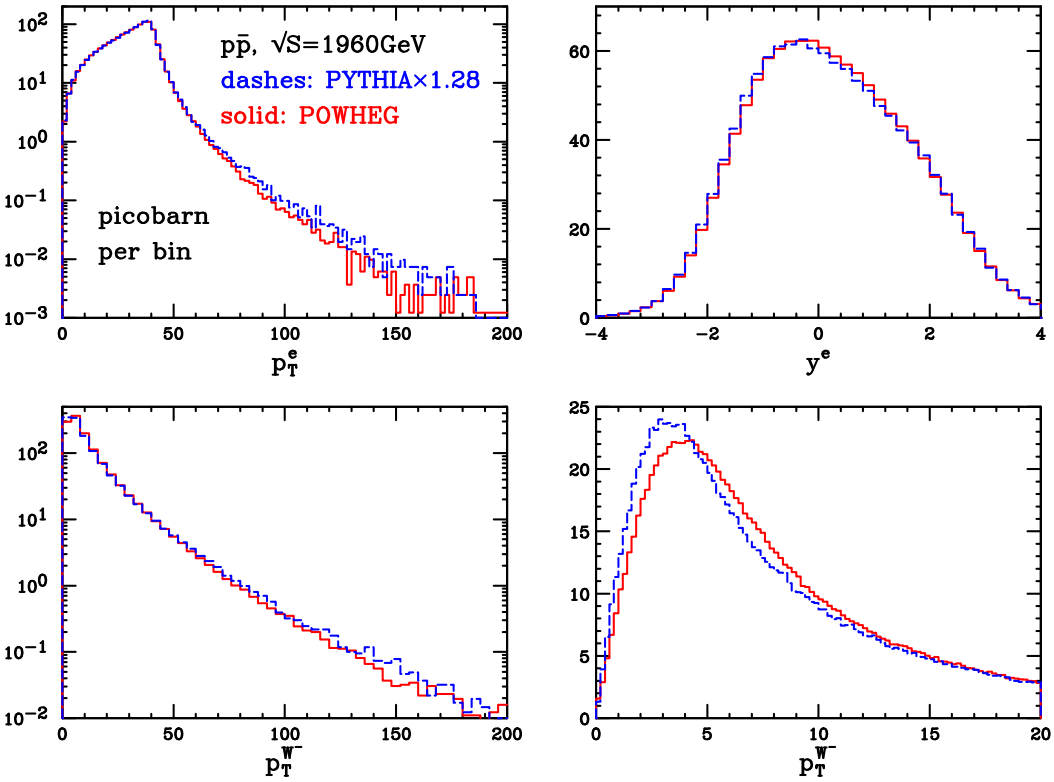

Figure 23: Same as figure 17 for a PYTHIA and POWHEG comparison at the Tevatron.

JHEP07(2008)060

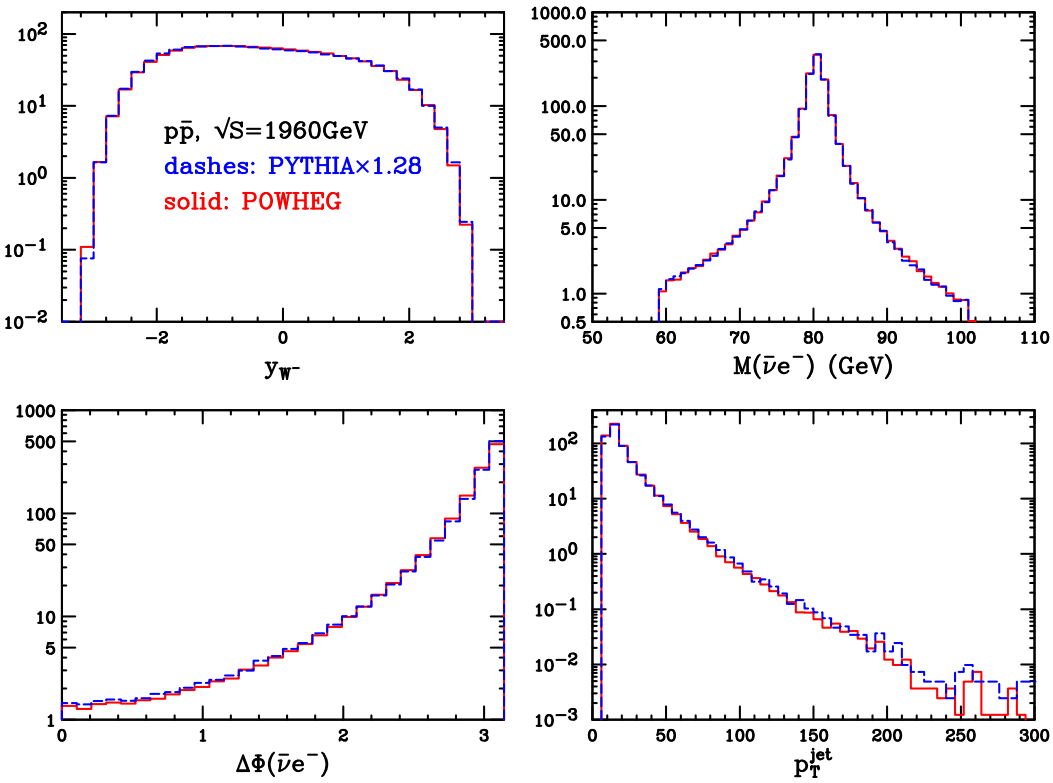

Figure 24: Same as figure 18 for a PYTHIA and POWHEG comparison at the Tevatron.

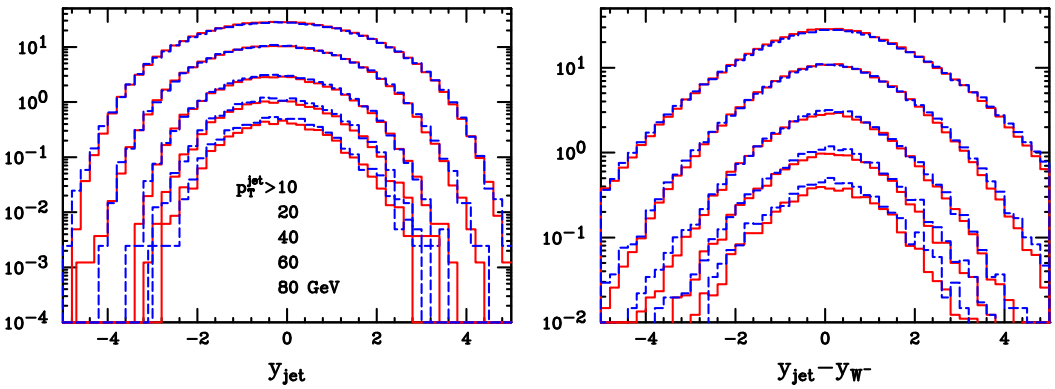

Figure 25: Same as figure 19 for a PYTHIA and POWHEG comparison at the Tevatron.

JHEP07(2008)060

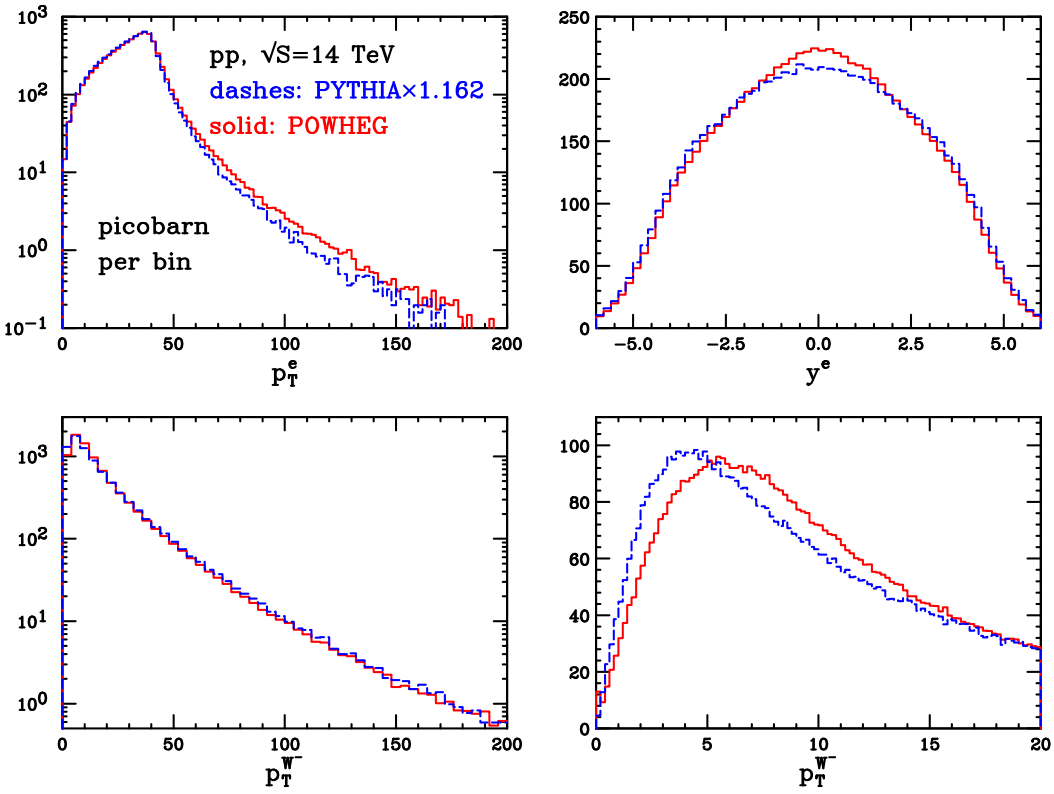

Figure 26: Same as figure 17 for a PYTHIA and POWHEG comparison at the LHC.

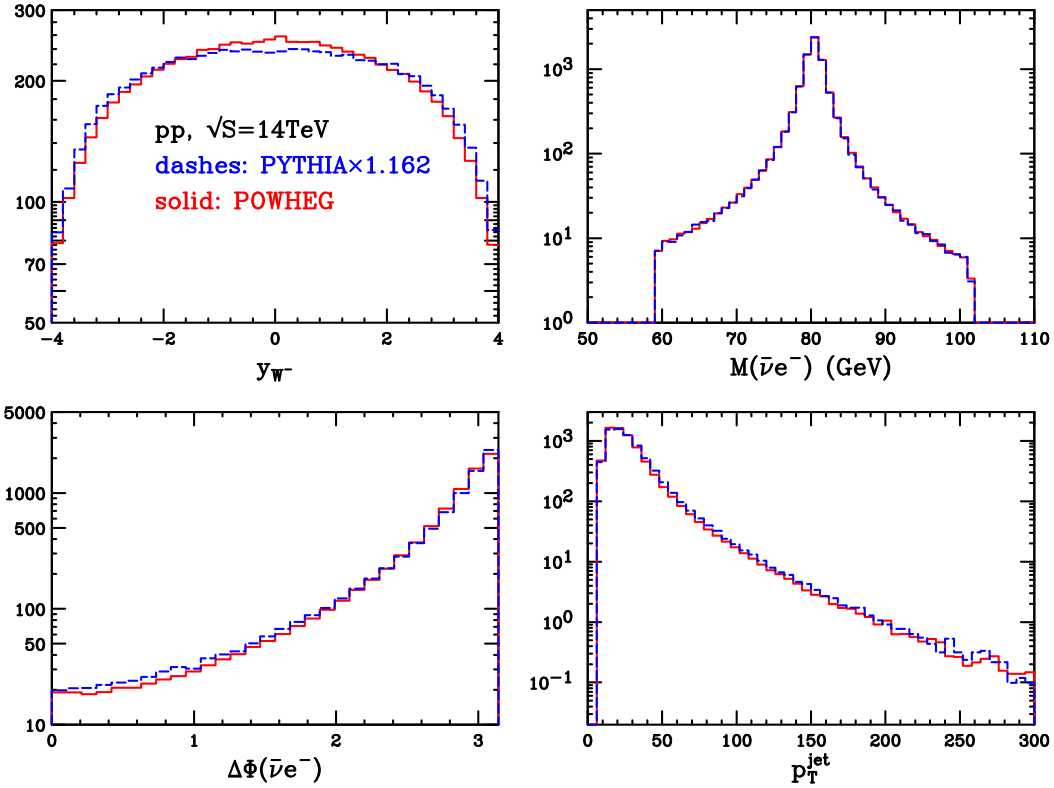

Figure 27: Same as figure 18 for a PYTHIA and POWHEG comparison at the LHC.

JHEP07(2008)060

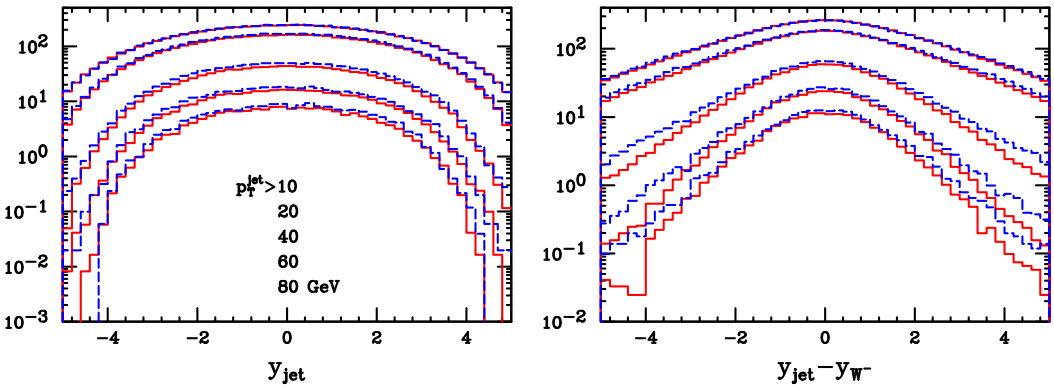

Figure 28: Same as figure 19 for a PYTHIA and POWHEG comparison at the LHC.

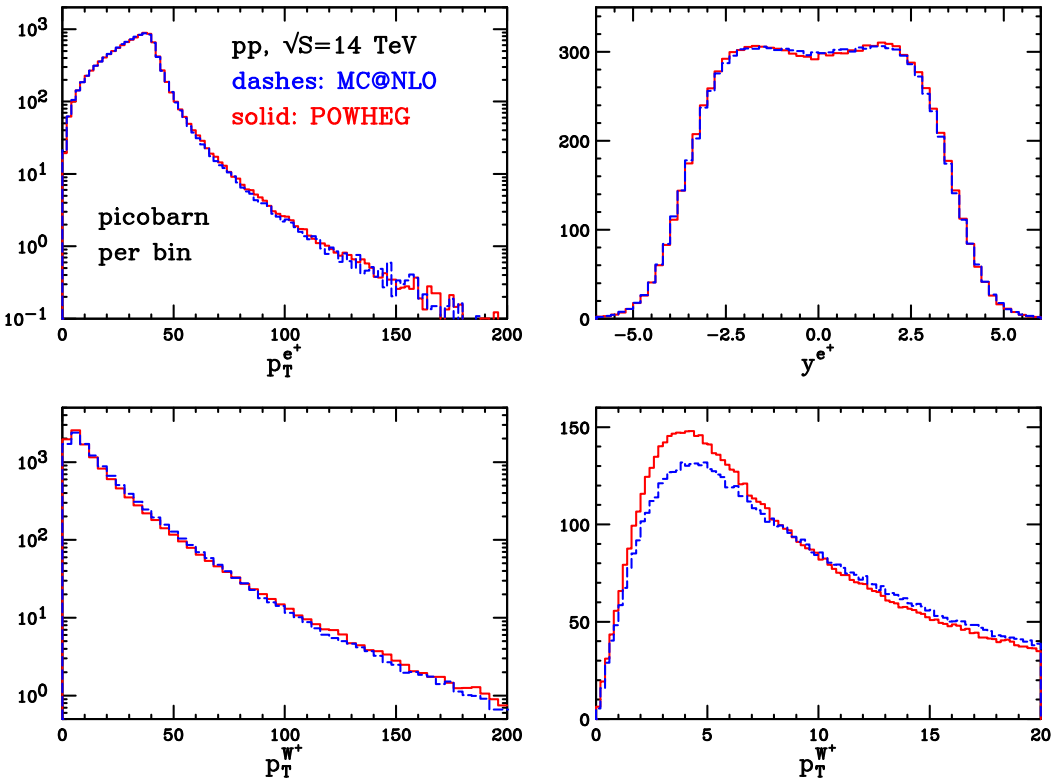

Figure 29: Same as figure 20 for W^+ production at the LHC.

5. Conclusions

In this paper we have reported on a complete implementation of vector-boson production at NLO in the POWHEG framework. The calculation was performed within the Catani-Seymour [6] dipole approach, and thus this is the first POWHEG implementation within the Catani-Seymour framework at a hadronic collider. We have found that, at variance with what was proposed in section 7.3 of ref. [5], it is better to define the transverse momentum as the true transverse momentum for the initial-state singular region. Furthermore, we have shown how to perform a POWHEG implementation when the Born term vanishes.

JHEP07(2008)060

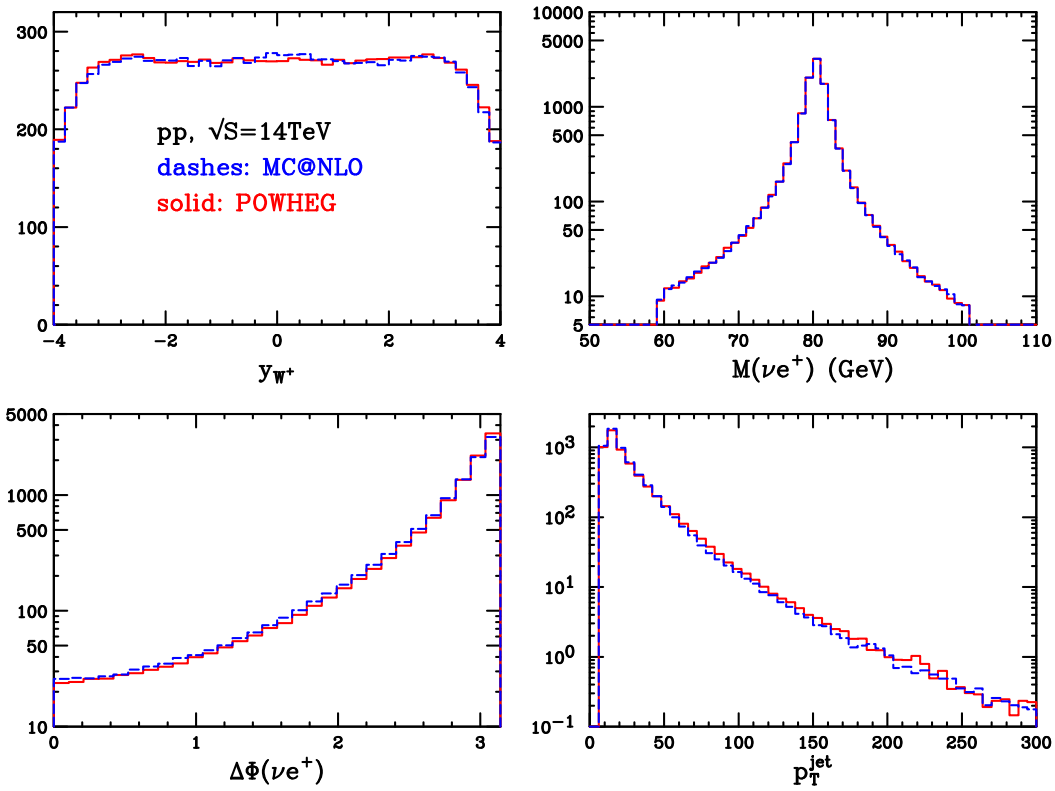

Figure 30: Same as figure 21 for W^+ production at the LHC.

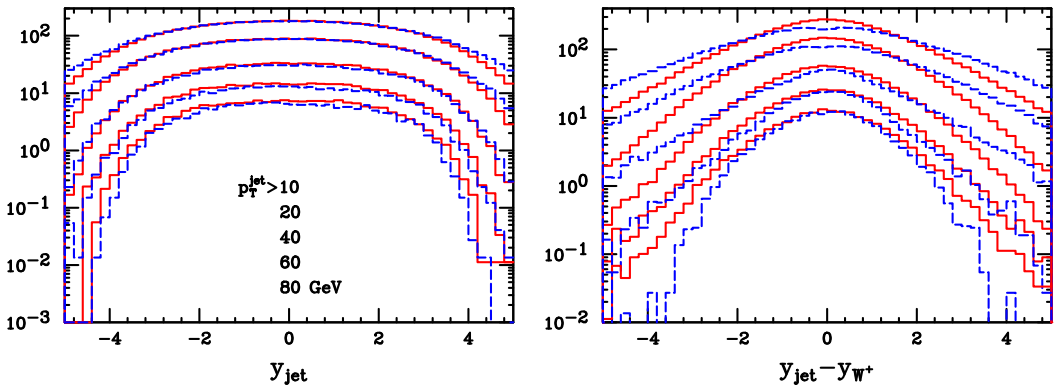

Figure 31: Same as figure 22 for W^+ production at the LHC.

The results of our work have been compare extensively with MC@NLO and PYTHIA. The PYTHIA result, rescaled to the full NLO cross section, is in good agreement with POWHEG, except for differences in the rapidity distribution of the vector boson, that may be ascribed to the use of a LO parton density in PYTHIA. The MC@NLO result is in fair agreement with POWHEG, except for the distribution of the hardest jet in the process, the MC@NLO distribution being generally wider. Furthermore, we have also examined the distributions in the difference of the hardest jet and the vector-boson rapidity. We have found that MC@NLO distributions exhibit dips at zero rapidity. We have also examined analogous distributions

JHEP07(2008)060

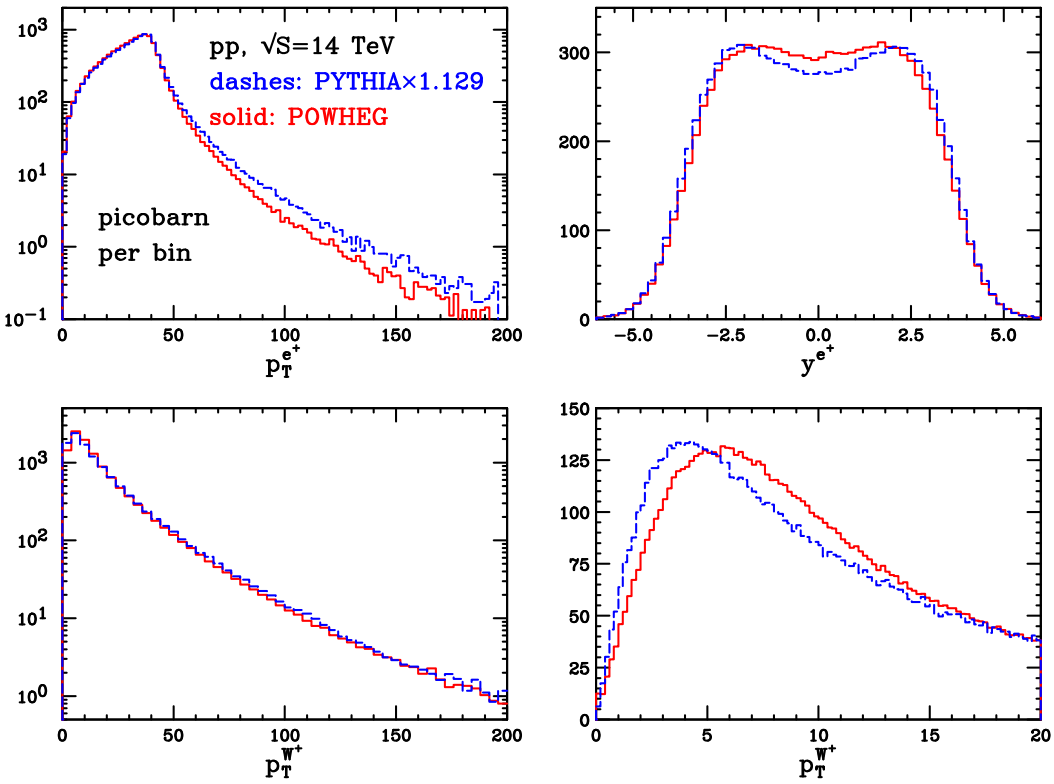

Figure 32: Same as figure 26 for W^+ production at the LHC.

for ZZ and $t\bar{t}$ production, and again found dips for these distributions, that seem to be a general feature of the MC@NLO approach. We also remark that no other approaches show dips of this kind [29].

The computer code for the POWHEG implementations presented here is available, together with the manual, at the site http://moby.mib.infn.it/∼nason/POWHEG/.

Acknowledgments

We wish to thank S. Frixione, K. Hamilton, T. Sjöstrand and B. Webber for useful discussions. This research was supported in part by the National Science Foundation under Grant No. PHY05-51164.

Right after completion of this work, another POWHEG implementation of vector-boson production has appeared in the literature [30].

A. Upper bounding function

We call $\Delta_U(p_T^2)$ the Sudakov form factor obtained with the upper bounding function of eq. (3.10). Using the definitions of eqs. (2.22) and (2.17)

$$d\Phi_{\rm rad} = \frac{M^2}{16\pi^2}\,\frac{d\phi}{2\pi}\,dv\,\frac{dx}{x^2}\,\theta(v)\,\theta\left(1-\frac{v}{1-x}\right)\theta(x(1-x))\,\theta(x-\bar{x}_\oplus) \qquad \text{(A.1)}$$

JHEP07(2008)060

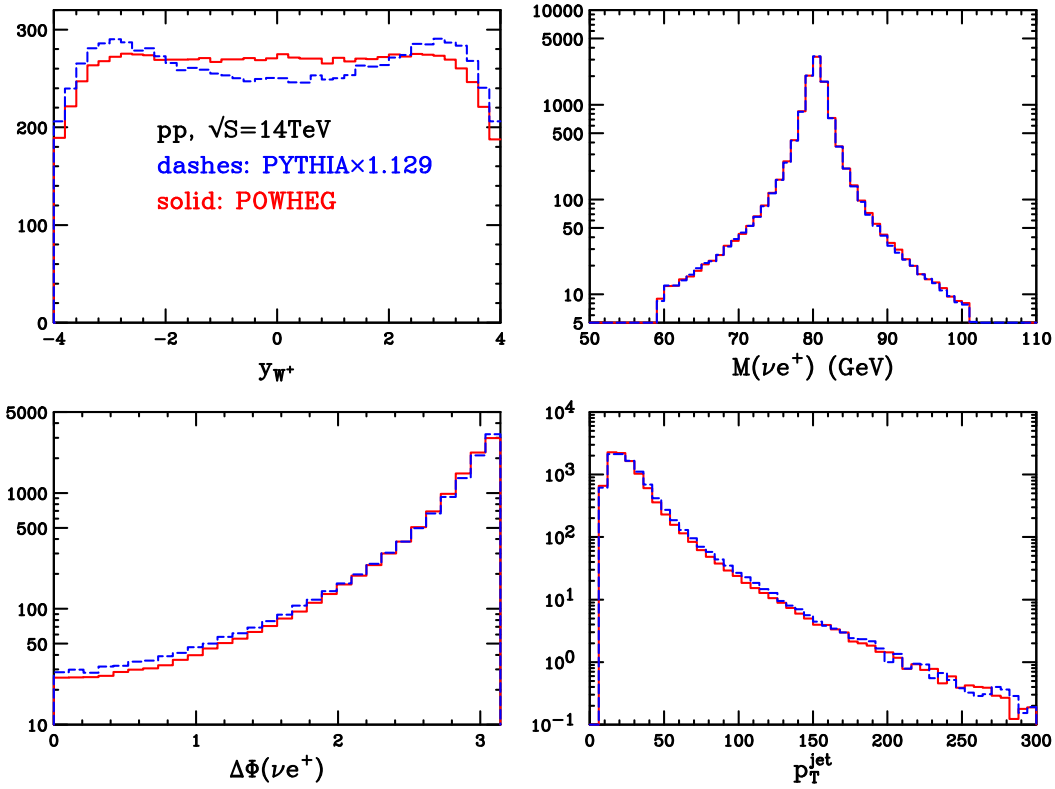

Figure 33: Same as figure 27 for W^+ production at the LHC.

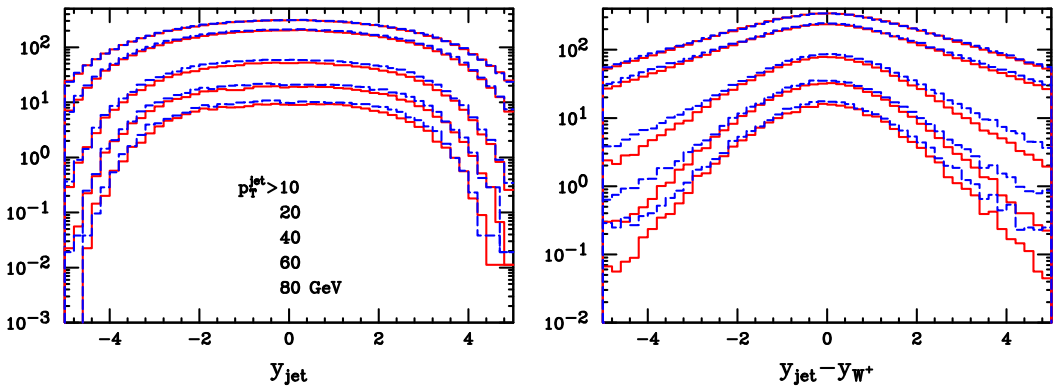

Figure 34: Same as figure 28 for W^+ production at the LHC.

$$k_T^2 = \frac{M^2}{x}(1-x-v)\,v\,, \tag{A.2}$$

we write

$$\begin{aligned}\frac{\log\Delta_U(p_T^2)}{-N} &= \int_{\bar{x}}^1 \frac{dx}{x^2}\int_0^{1-x} dv\,\frac{\alpha_s(k_T^2)}{2v}\,\frac{x^2}{1-x-v}\,\theta\big(k_T^2-p_T^2\big)\\ &= \int_{\bar{x}}^1 \frac{dx}{x}\int_0^{1-x} dv\,\frac{\alpha_s(k_T^2)}{2}\,\frac{M^2}{k_T^2}\,\theta\big(k_T^2-p_T^2\big)\end{aligned}$$

JHEP07(2008)060

$$= \int_{p_T^2}^{\infty} \frac{dk_T^2}{k_T^2} \frac{\alpha_s(k_T^2)}{2} \int_0^1 dv \int_{\bar{x}}^1 \frac{dx}{x} \theta(1-x-v)\, M^2\, \delta\!\left(\frac{M^2}{x}(1-x-v)v - k_T^2\right),$$

where, for ease of notation, we have dropped the $\circledast$ and $q\bar{q}$ labels on N and $\bar{x}$. We perform the x integration using the δ function

$$\int \frac{dx}{x}\, M^2\, \delta\!\left(\frac{M^2}{x}(1-x-v)v - k_T^2\right) = \frac{1}{k_T^2/M^2 + v}, \qquad x = \frac{M^2 v(1-v)}{k_T^2 + M^2 v}\,. \tag{A.3}$$

Notice that $x < 1$, and

$$\theta\!\left(1 - v - \frac{M^2 v(1-v)}{k_T^2 + M^2 v}\right) = \theta\!\left(1 - v\frac{k_T^2 + M^2}{k_T^2 + M^2 v}\right) = 1. \tag{A.4}$$

The only remaining condition on x is $x \geqslant \bar{x}$. We thus get

$$\frac{\log \Delta_U(p_T^2)}{-N} = \int_{p_T^2}^{\infty} \frac{dk_T^2}{k_T^2} \frac{\alpha_s(k_T^2)}{2} \int_0^1 \frac{dv}{k_T^2/M^2 + v}\, \theta\!\left(\frac{M^2 v(1-v)}{k_T^2 + M^2 v} - \bar{x}\right). \tag{A.5}$$

We must find the conditions implied by the theta function upon v. For

$$k_T^2 < k_{T\,\max}^2 = \frac{M^2(1-\bar{x})^2}{4\bar{x}}\,, \tag{A.6}$$

the θ function is satisfied if $v_- < v < v_+$, where

$$v_\pm = \frac{1 - \bar{x} \pm \sqrt{(1-\bar{x})^2 - 4\,\bar{x}\,\frac{k_T^2}{M^2}}}{2}\,. \tag{A.7}$$

We thus have

$$\frac{\log \Delta_U(p_T^2)}{-N} = \int_{p_T^2}^{k_{T\,\max}^2} \frac{dk_T^2}{k_T^2} \frac{\alpha_s(k_T^2)}{2} \log \frac{\frac{k_T^2}{M^2} + v_+}{\frac{k_T^2}{M^2} + v_-}\,. \tag{A.8}$$

The k_T^2 integral is still too complex to be performed analytically. We thus resort another time to the veto method, by finding an upper bound to the integrand. We have

$$\frac{\frac{k_T^2}{M^2} + v_+}{\frac{k_T^2}{M^2} + v_-} \leqslant \frac{\frac{k_T^2}{M^2} + 1}{\frac{k_T^2}{M^2}} = \frac{M^2}{k_T^2} + 1 \leqslant \frac{M^2}{k_T^2} + \frac{k_{T\,\max}^2}{k_T^2} = \frac{M^2(1+\bar{x})^2}{4\,\bar{x}\,k_T^2}. \tag{A.9}$$

We thus define

$$q^2 = \frac{M^2(1+\bar{x})^2}{4\,\bar{x}\,k_T^2}, \tag{A.10}$$

and introduce a new Sudakov form factor

$$\frac{\log \tilde{\Delta}_U(p_T^2)}{-N} = \int_{p_T^2}^{k_{T\,\max}^2} \frac{dk_T^2}{k_T^2} \frac{\alpha_U(k_T^2)}{2} \log \frac{q^2}{k_T^2}, \tag{A.11}$$

where $\alpha_U(k_T^2)$ has the form of the one-loop running coupling constant

$$\alpha_U(k_T^2) = \frac{1}{b \log \frac{k_T^2}{\Lambda_U^2}}, \tag{A.12}$$

and is required to satisfy the bound $\alpha_U(k_T^2) \geqslant \alpha_s(k_T^2)$ in the allowed range for k_T^2. The integral in eq. (A.11) is now easily performed, and we get

$$\tilde{\Delta}_U(p_T^2) = \exp\left\{-\frac{N}{2b}\left[\log\frac{q^2}{\Lambda_U^2}\log\frac{\log\frac{k_{T\,\max}^2}{\Lambda_U^2}}{\log\frac{p_T^2}{\Lambda_U^2}} - \log\frac{k_{T\,\max}^2}{p_T^2}\right]\right\}. \tag{A.13}$$

The generation of the radiation variables is then performed starting with $\tilde{\Delta}_U(p_T^2)$, using the veto procedure to obtain the $\Delta_U(p_T^2)$ distribution. Further vetoing is then used to obtain the correct R/B generated distribution.

References

[1] P. Nason, *A new method for combining NLO QCD with shower Monte Carlo algorithms*, *JHEP* **11** (2004) 040 [hep-ph/0409146].

[2] P. Nason and G. Ridolfi, *A positive-weight next-to-leading-order Monte Carlo for Z pair hadroproduction*, *JHEP* **08** (2006) 077 [hep-ph/0606275].

[3] S. Frixione, P. Nason and G. Ridolfi, *A positive-weight next-to-leading-order Monte Carlo for heavy flavour hadroproduction*, *JHEP* **09** (2007) 126 [arXiv:0707.3088].

[4] O. Latunde-Dada, S. Gieseke and B. Webber, *A positive-weight next-to-leading-order Monte Carlo for e^+e^- annihilation to hadrons*, *JHEP* **02** (2007) 051 [hep-ph/0612281].

[5] S. Frixione, P. Nason and C. Oleari, *Matching NLO QCD computations with parton shower simulations: the POWHEG method*, *JHEP* **11** (2007) 070 [arXiv:0709.2092].

[6] S. Catani and M.H. Seymour, *A general algorithm for calculating jet cross sections in NLO QCD*, *Nucl. Phys.* **B 485** (1997) 291 [*Erratum ibid.* **B 510** (1998) 503] [hep-ph/9605323].

[7] S. Frixione, Z. Kunszt and A. Signer, *Three-jet cross sections to next-to-leading order*, *Nucl. Phys.* **B 467** (1996) 399 [hep-ph/9512328].

[8] S. Frixione, *A general approach to jet cross sections in QCD*, *Nucl. Phys.* **B 507** (1997) 295 [hep-ph/9706545].

[9] S. Frixione and B.R. Webber, *Matching NLO QCD computations and parton shower simulations*, *JHEP* **06** (2002) 029 [hep-ph/0204244].

[10] T. Sjöstrand, S. Mrenna and P. Skands, *PYTHIA* 6.4 *physics and manual*, *JHEP* **05** (2006) 026 [hep-ph/0603175].

[11] K. Hagiwara and D. Zeppenfeld, *Helicity amplitudes for heavy lepton production in e^+e^- annihilation*, *Nucl. Phys.* **B 274** (1986) 1.

[12] K. Hagiwara and D. Zeppenfeld, *Amplitudes for multiparton processes involving a current at e^+e^-, $e^\pm p$ and hadron colliders*, *Nucl. Phys.* **B 313** (1989) 560.

[13] F. Maltoni and T. Stelzer, *MadEvent: automatic event generation with MadGraph*, *JHEP* **02** (2003) 027 [hep-ph/0208156].

[14] S. Kawabata, *A new version of the multidimensional integration and event generation package BASES/SPRING*, *Comput. Phys. Commun.* **88** (1995) 309.

JHEP07(2008)060

[15] P. Nason, *MINT: a computer program for adaptive Monte Carlo integration and generation of unweighted distributions*, arXiv:0709.2085.

[16] G. Corcella et al., *HERWIG* 6*: an event generator for hadron emission reactions with interfering gluons (including supersymmetric processes)*, *JHEP* **01** (2001) 010 [hep-ph/0011363].

[17] G. Corcella et al., *HERWIG* 6.5 *release note*, hep-ph/0210213.

[18] J. Pumplin et al., *New generation of parton distributions with uncertainties from global QCD analysis*, *JHEP* **07** (2002) 012 [hep-ph/0201195].

[19] G.P. Salam and G. Soyez, *A practical seedless infrared-safe cone jet algorithm*, *JHEP* **05** (2007) 086 [arXiv:0704.0292].

[20] M. Cacciari and G.P. Salam, *Dispelling the N^3 myth for the k_t jet-finder*, *Phys. Lett.* **B 641** (2006) 57 [hep-ph/0512210].

[21] M.L. Mangano, M. Moretti, F. Piccinini and M. Treccani, *Matching matrix elements and shower evolution for top-quark production in hadronic collisions*, *JHEP* **01** (2007) 013 [hep-ph/0611129].

[22] M. Bengtsson and T. Sjöstrand, *Coherent parton showers versus matrix elements: implications of PETRA - PEP data*, *Phys. Lett.* **B 185** (1987) 435.

[23] T. Sjöstrand, *Monte Carlo generators*, hep-ph/0611247.

[24] C. Anastasiou, L.J. Dixon, K. Melnikov and F. Petriello, *High-precision QCD at hadron colliders: electroweak gauge boson rapidity distributions at NNLO*, *Phys. Rev.* **D 69** (2004) 094008 [hep-ph/0312266].

[25] D0 collaboration, V.M. Abazov et al., *Measurement of the shape of the boson transverse momentum distribution in $p\bar{p} \to Z/\gamma^* \to e^+e^- + X$ events produced at $\sqrt{s} = 1.96$ TeV*, *Phys. Rev. Lett.* **100** (2008) 102002 [arXiv:0712.0803].

[26] CDF collaboration, A.A. Affolder et al., *The transverse momentum and total cross section of e^+e^- pairs in the Z boson region from $p\bar{p}$ collisions at $\sqrt{s} = 1.8$ TeV*, *Phys. Rev. Lett.* **84** (2000) 845 [hep-ex/0001021].

[27] D0 collaboration, B. Abbott et al., *Measurement of the inclusive differential cross section for Z bosons as a function of transverse momentum in $\bar{p}p$ collisions at $\sqrt{s} = 1.8$ TeV*, *Phys. Rev.* **D 61** (2000) 032004 [hep-ex/9907009].

[28] D0 collaboration, B. Abbott et al., *Differential production cross section of Z bosons as a function of transverse momentum at $\sqrt{s} = 1.8$ TeV*, *Phys. Rev. Lett.* **84** (2000) 2792 [hep-ex/9909020].

[29] J. Alwall et al., *Comparative study of various algorithms for the merging of parton showers and matrix elements in hadronic collisions*, *Eur. Phys. J.* **C 53** (2008) 473 [arXiv:0706.2569].

[30] K. Hamilton, P. Richardson and J. Tully, *A positive-weight next-to-leading order Monte Carlo simulation of Drell-Yan vector boson production*, arXiv:0806.0290.

JHEP07(2008)060